JGR Oceans

RESEARCH ARTICLE
10.1029/2022JC019622

Parametric Subharmonic Instability of the M_2 Internal Tides in the Tokara Strait

Shuya Wang[1], Xinyu Guo[1], Anzhou Cao[2], Eisuke Tsutsumi[3], and Xu Chen[4]

[1]Center for Marine Environmental Studies, Ehime University, Matsuyama, Japan, [2]Ocean College, Zhejiang University, Zhoushan, China, [3]Faculty of Fisheries, Kagoshima University, Kagoshima, Japan, [4]Key Laboratory of Physical Oceanography, Ocean University of China, Qingdao, China

Abstract The Tokara Strait is a mixing hotspot due to the coexistence of complex bottom topographies and strong composite flow including both the Kuroshio and tidal currents. Although previous studies have revealed several mechanisms from the view of Kuroshio-Topography interaction, the role of tides in driving mixing is still not clear. Given that it is located at the M_2 critical latitude (29°N), parametric subharmonic instability (PSI) is expected as an important process responsible for the mixing. Here, we study PSI of the M_2 internal tides in the Tokara Strait based on a high-resolution model. Our model results indicate that intense near-inertial waves are generated via PSI, which exhibit a horizontally layered structure and have much larger vertical wavenumbers than the M_2 internal tides. Energy is transferred from the M_2 internal tides to the near-inertial waves around the generation sites, and most of the near-inertial energy is dissipated locally. The dissipation rates of near-inertial waves are comparable to those of the M_2 internal tides. Simulations with and without the Kuroshio Current revealed the suppression of PSI along the Kuroshio path, which could be attributed to two mechanisms. First, the Kuroshio Current modifies the local minimum internal wave frequency by its horizontal and vertical shear, making the condition for PSI not satisfied. Second, the Kuroshio Current advects the near-inertial waves downstream in the Okinawa Trough, which inhibits the accumulation of near-inertial energy there. However, in most of the areas outside the Kuroshio path, PSI majorly contributes to mixing in and around the Tokara Strait.

Plain Language Summary The Tokara Strait is the passage of the Kuroshio Current from the East China Sea to the Western Pacific, which is characterized by complex bottom topographies and strong turbulent mixing. By conducting numerical simulations, we find that intense nonlinear wave-wave interaction occurs in the Tokara Strait, since it is exactly located at the M_2 critical latitude where the local inertial frequency is equal to half of the M_2 tidal frequency. Such nonlinear wave-wave interaction gives rise to high-wavenumber internal waves at inertial frequency, causing elevated energy dissipation. By performing the sensitivity experiment without the Kuroshio Current, we further reveal that the Kuroshio Current suppresses the above nonlinear energy transfer process specifically along its path because it changes the lower limit of internal wave frequency via sheared currents and advects the near-inertial energy downstream in a shorter time scale. Our results reveal an important process responsible for mixing in and around the Tokara Strait and help us understand the energy cascade of internal tides in the ocean.

Key Points:

- Parametric subharmonic instability (PSI) of the M_2 internal tides in the Tokara Strait generates small-scale near-inertial waves
- Internal tidal energy is transferred to near-inertial waves around generation sites via PSI and most of it is dissipated locally
- The Kuroshio Current weakens PSI by changing the minimum wave frequency, causing an advection effect

Supporting Information:

Supporting Information may be found in the online version of this article.

Correspondence to:

X. Guo,
guo.xinyu.mz@ehime-u.ac.jp

Citation:

Wang, S., Guo, X., Cao, A., Tsutsumi, E., & Chen, X. (2024). Parametric subharmonic instability of the M_2 internal tides in the Tokara Strait. *Journal of Geophysical Research: Oceans*, *129*, e2022JC019622. https://doi.org/10.1029/2022JC019622

Received 27 DEC 2022
Accepted 20 OCT 2024

Author Contributions:

Conceptualization: Shuya Wang
Data curation: Xinyu Guo
Formal analysis: Shuya Wang
Funding acquisition: Xinyu Guo, Anzhou Cao
Investigation: Shuya Wang, Anzhou Cao, Eisuke Tsutsumi
Methodology: Shuya Wang, Anzhou Cao
Software: Shuya Wang
Supervision: Xinyu Guo
Validation: Shuya Wang
Visualization: Shuya Wang
Writing – original draft: Shuya Wang
Writing – review & editing: Shuya Wang, Xinyu Guo, Anzhou Cao, Eisuke Tsutsumi, Xu Chen

1. Introduction

Internal tides are internal waves at the tidal frequencies. As barotropic tidal currents flow over rough topographies (e.g., seamounts, mid-ocean ridges, and continental slopes), they push the stratified water up and down to generate internal tides (Garrett & Kunze, 2007). Near the generation sites, internal tides exhibit beam-like structures (Cole et al., 2009; Pickering & Alford, 2012). In the far field, internal tides are dominated by low modes that can propagate over 1,000 km in the open ocean (Alford, 2003; Zaron, 2019; Zhao et al., 2016). Breaking of internal tides significantly contributes to turbulent mixing in the ocean, especially in the near-bottom regions (Garrett, 2003; Jayne et al., 2004; St. Laurent & Garrett, 2002; Vic et al., 2019), which is essential for the maintenance of the global meridional overturning circulation (Munk & Wunsch, 1998; Oka & Niwa, 2013). The total energy conversion from barotropic tides to internal tides is estimated to be approximately 1 TW (Niwa & Hibiya, 2011; Simmons et al., 2004). Understanding how the internal tidal energy is dissipated is of vital importance because it is necessary for improving the parameterizations on the internal tide-driven mixing in climate models (Mackinnon et al., 2017; Whalen et al., 2020).

Parametric subharmonic instability (PSI) has been considered as one of the important ways of removing energy from internal tides (Hibiya et al., 1998, 2002). PSI is a special kind of nonlinear resonant triad interaction that transfers internal tidal energy to two subharmonic waves at nearly half the tidal frequency (McComas & Bretherton, 1977). In this triad, the wave frequencies ω and wavenumbers $\mathbf{k}$ satisfy the following conditions:

$$\omega_0 = \omega_1 + \omega_2 \tag{1}$$

and

$$\mathbf{k}_0 = \mathbf{k}_1 + \mathbf{k}_2, \tag{2}$$

where the subscripts 0, 1, and 2 denote the "parent wave" (internal tides) and two "daughter waves" (subharmonic waves), respectively. In theory, PSI of internal tides is most efficient at the "critical latitude," where the local inertial frequency is equal to half the tidal frequency (14.5° for the K_1 internal tides and 28.9° for the M_2 internal tides). Such latitude-dependence of PSI has been confirmed by field observations, of which the results demonstrate enhanced turbulent mixing at the critical latitude (Alford, 2008; Alford et al., 2007; Hibiya & Nagasawa, 2004; Hibiya et al., 2006, 2007; MacKinnon, Alford, Pinkel, et al., 2013; Nagasawa et al., 2002). Motivated by the above results, the following observations based on long-term velocity measurements record small-scale near-inertial waves propagating both upward and downward, which is a typical feature of PSI (Girton et al., 2011; MacKinnon, Alford, Sun, et al., 2013). Furthermore, the energy transfer from internal tides into the subharmonic waves via PSI is considerably affected by background currents (Yang et al., 2020).

Numerical simulation is another approach for exploring PSI. Using a two-dimensional model, Hibiya et al. (1998, 2002) pointed out that PSI largely controls the downscaled energy cascade from low-mode internal tides to mixing. MacKinnon and Winters (2005) predicted considerable energy loss via PSI when internal tides propagate poleward across the critical latitude. In the subsequent work, Hazewinkel and Winters (2011) used vertically nonuniform stratification in their model and suggested that the generation of near-inertial waves by PSI of internal tides mainly occurs in the upper ocean. Other simulations with varying bottom topographies and barotropic tidal forcing further indicated that PSI can occur near the generation sites of internal tides, thereby elevating the local dissipation of internal tidal energy (e.g., Gerkema et al., 2006; Nikurashin & Legg, 2011; Richet et al., 2018; Wang, Cao, Chen, et al., 2021).

In addition to idealized experiments, numerical simulations with realistic forcing and topographies are performed to examine the intensity of PSI in the ocean. Simmons (2008) first showed the spatial pattern of subharmonic M_1 internal tides excited by PSI of the M_2 internal tides in the global ocean with an isopycnal coordinate model. Ansong et al. (2018) considered atmospheric forcing and subtidal circulations in the global ocean model, and claimed that the energy transfer rates from internal tides into subharmonic waves are actually dependent on model resolution; that is, a finer horizontal resolution would result in higher energy transfer rates. Liu and Zhao (2020) focused on PSI of the K_1 internal tides in the South China Sea. Their model results revealed that the K_1 critical latitude at 14°N in the central South China Sea behaves as an "island chain" radiating high-mode subharmonic waves equatorward.

The Tokara Strait is located south of the Kyushu Island, through which the Kuroshio Current flows from the East China Sea into the Western Pacific. This region is characterized by complex bottom topographies in the presence of many islands and seamounts. Strong turbulent mixing has been observed in the Tokara Strait, with the diapycnal diffusivity as high as 10^{-3}–10^{-2} m^2/s (Hasegawa et al., 2021; Nagai et al., 2017, 2021; Tsutsumi et al., 2017). The Tokara Strait is also a hotspot for internal tide generation in the Western Pacific (Figure 1a). Numerical model results suggest that 3.8–9.3 GW energy of the M_2 barotropic tides is converted into internal tides in the Tokara Strait (Niwa & Hibiya, 2004; Varlamov et al., 2015), nearly comparable to those in other major generation sites of internal tides in the Western Pacific, such as the Izu-Ogasawara ridge, and the Mariana Arc (Kerry et al., 2013; Varlamov et al., 2015; Wang et al., 2018). Considering that the Tokara Strait is located at the M_2 critical latitude (Figure 1a), intense PSI of the M_2 internal tides is expected. However, up to now, PSI of the M_2 internal tides in the Tokara Strait has not been reported, providing us with the motivation for this study.

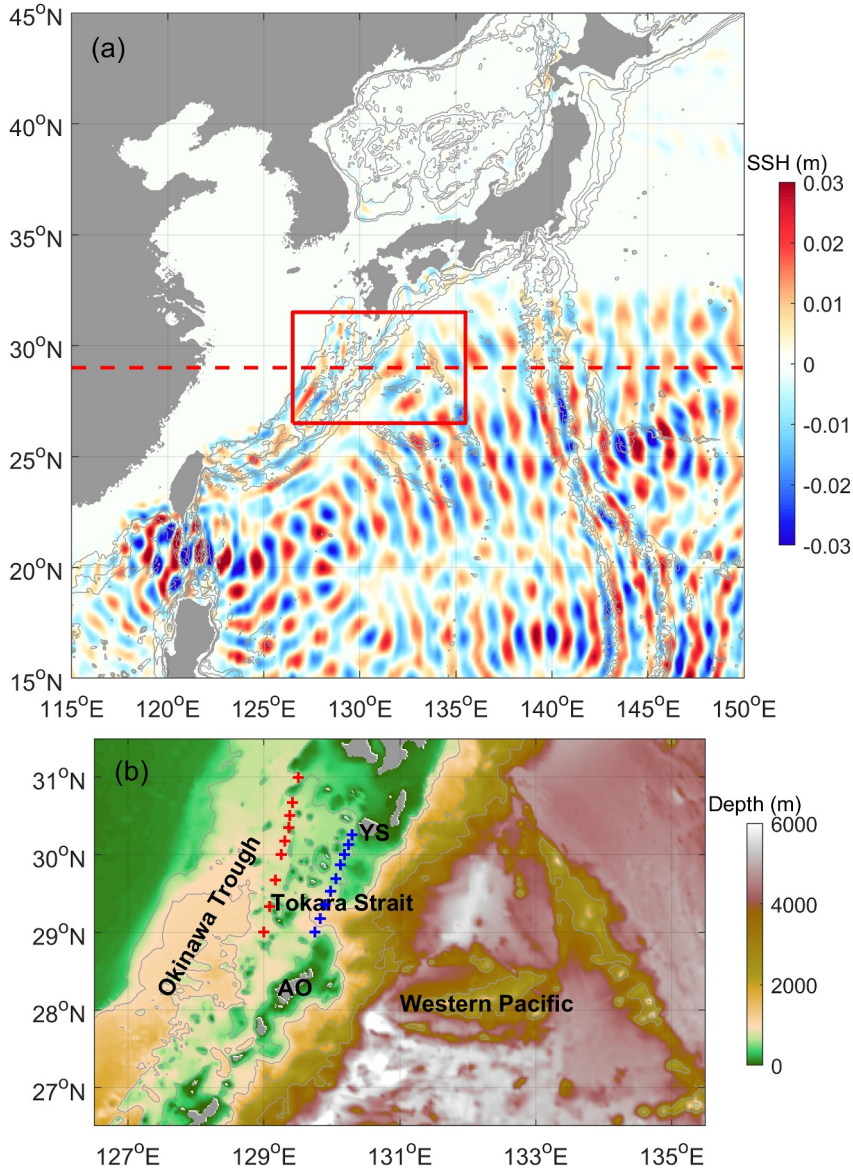

Figure 1. (a) Sea surface heights (shading, unit: m) of the M_2 internal tides in the Western Pacific from Zaron (2019). The model domain in this study is indicated by the red rectangle. The M_2 critical latitude is denoted by the red dashed line. (b) Bathymetry in the model domain (shading, unit: m). Stations of microstructure measurements are indicated by red (Transect I) and blue crosses (Transect II). "YS" and "AO" are short for Yakushima Island and Amami-oshima Island, respectively. Gray contours in panels (a) and (b) show 500, 1,000, 2,000, and 3,000 m isobaths.

In this study, PSI of the M_2 internal tides in the Tokara Strait is investigated using a high-resolution numerical model. Our goal is to provide a comprehensive insight into the physical process and energetics of PSI of the M_2 internal tides in the Tokara Strait. The remainder of this paper is organized as follows. The model configuration and validation are presented in Section 2. In Section 3, the basic characteristics of the M_2 internal tides in this region are shown. Then we analyze PSI of the M_2 internal tide. Characteristics and energetics of the near-inertial waves excited by PSI are the main focus. In Section 4, the influence of Kuroshio Current on PSI is explored. In Section 5, we further discuss the evolution of PSI-generated near-inertial waves and the implications of this study. Finally, Section 6 summarizes this paper.

2. Methodology

2.1. Model Setup

In this study, the MIT general circulation model (MITgcm, Marshall et al., 1997) is employed. The MITgcm solves the three-dimensional Navier-Stokes equation with the Boussinesq approximation, thermodynamic equation, and salinity equation using the finite-volume method. The equations are solved on a spherical coordinate system with the traditional approximation made for the Coriolis effect (Delorme & Thomas, 2023; Gerkema & Zimmerman, 2008). Here, the model is configured in hydrostatic mode, because the horizontal scales of both the internal tides and PSI-generated near-inertial waves are much larger than the vertical scales. The model domain is shown in Figure 1b. Bathymetry is extracted from the ETOPO1 data set, and the maximum depth is set to 6,000 m. The horizontal resolution of our model is set to 1/60° (~1.8 km), which is sufficiently high for studying PSI according to previous numerical studies (Ansong et al., 2018; Liu & Zhao, 2020). There are 70 uneven layers in the vertical direction, whose thickness increases from 5 m near the surface to 250 m near the bottom. The total grid numbers are $540 \times 300 \times 70$. Constant horizontal and vertical viscosities (diffusivities) of $A_H = 10$ ($K_H = 10^{-3}$) m^2/s and $A_V = 10^{-3}$ ($K_V = 10^{-5}$) m^2/s are used. These values are chosen empirically based on previous studies (e.g., Nagai & Hibiya, 2015; Tanaka et al., 2010) to eliminate grid-scale noise. Because of the great change of water depth in our model domain, we could not incorporate the GM background internal waves as Iwamae and Hibiya (2012). The quadratic scheme is considered for bottom friction, with $C_d = 2.5 \times 10^{-3}$. No-slip condition is applied to the bottom boundary, whereas free-slip condition is used for the lateral boundaries. Moreover, sponge layers are added to the lateral open boundaries to avoid the artificial reflection of baroclinic waves.

Given the coexistence of both the Kuroshio Current and tidal currents in the Tokara Strait, three numerical experiments are conducted in this study.

1. **Run-TK**: In this case, we consider the realistic ocean conditions including both the Kuroshio Current and tidal currents. Climatological fields from the Four-dimensional Variational Ocean Reanalysis (FORA, Usui et al., 2017) are used as initial and boundary conditions. The M_2 tidal forcing is imposed at lateral open boundaries using barotropic tidal currents predicted by the Oregon State University Tidal Inversion Software (OTIS, Egbert & Erofeeva, 2002).
2. **Run-T**: The case is initialized with horizontally uniform stratification derived from the World Ocean Atlas 2013 (See Supporting Information S1). Only the M_2 tidal forcing is imposed and no background currents are considered.
3. **Run-K**: The setup of this case is almost the same as that for Run-TK except that the M_2 tidal forcing is excluded.

All the above simulations are operated for 150 days with a time step of 30 s. The model results are saved hourly.

2.2. Model Validation (Run-TK)

First, the simulated M_2 barotropic tide is compared with that calculated by the OTIS. As shown in Figures 2a and 2b, the simulated amplitudes and phases of the M_2 barotropic tide agree well with those from the OTIS. The mean absolute errors of amplitudes and phases over the domain are 2.9 cm and 3.2°, respectively. Both the simulated and OTIS results indicate an increase in amplitude when the M_2 barotropic tide propagates from the deep western Pacific onto the shallow East China Sea shelf. In addition, small-scale fluctuations superposed on the co-phase lines are found in the model results (Figure 2a), reflecting the modulation of internal tides on barotropic tides (Jan et al., 2007; Zhao, 2014). The simulated M_2 barotropic tides are further validated through a comparison with the amplitude and phase from tidal gauge data using harmonic analysis (Figures 2c and 2d).

Second, the simulated M_2 internal tides are validated by comparison with the altimetry results from Zaron (2019). Following Zhao et al. (2010), we calculate the baroclinic sea surface heights (SSHs) corresponding to the M_2 internal tides. On the whole, the SSHs of the M_2 internal tides from our simulated results show a similar pattern to those from Zaron (2019) (Figures 2e and 2f). However, the simulated wavefield is somewhat stronger than the altimetry one. Several reasons may lead to the discrepancy in the intensity of internal tides, such as the lack of wave drag in the model (Zhao et al., 2016) and the underestimation of altimetry data caused by nontidal noise (Zhao, 2019). These comparisons make us to believe that the model we configured could be an effective tool for exploring PSI of the M_2 internal tides in this region.

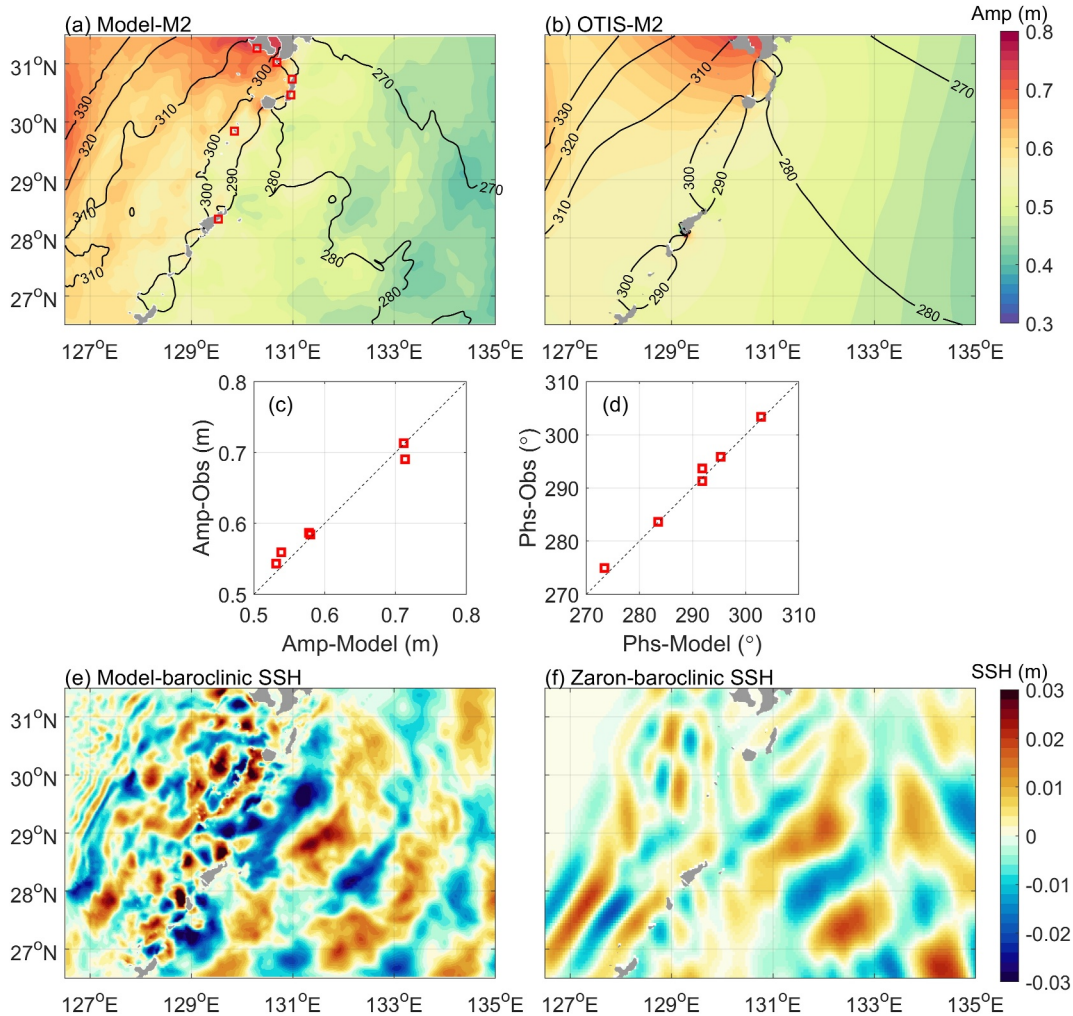

Figure 2. Co-tidal charts of the M_2 barotropic tide from (a) the model and (b) OTIS results. Amplitudes are indicated by shadings (unit: m) and phases by contours (unit: °). The red squares in panel (a) indicate the locations of tidal gauges. Comparison of modeled and observed (c) amplitudes and (d) phases of the M_2 barotropic tides at tidal gauges. Baroclinic sea surface heights (shading, unit: m) of the M_2 internal tides from (e) model results and (f) Zaron (2019). The model results are from Run-TK.

3. Results

3.1. Basic Characteristics of M_2 Internal Tides (Run-TK)

We first show the basic characteristics of the M_2 internal tides in this region. The presence of steep continental slope and strong tidal currents make the Tokara Strait a hotspot for internal tides in the Western Pacific, which has been presented in previous studies (Niwa & Hibiya, 2004; Tsutsumi et al., 2017; Varlamov et al., 2015). The tidal velocity $\widetilde{\mathbf{u}}_T$ is extracted by applying a fourth-order Butterworth filter within a frequency band of [1.73 2.13] cpd in a Eulerian framework. Although the Lagrangian filter has better performance in separating waves from background currents, the small domain with a strong mean flow causes difficulty in filtering variables for particles because the particles will reach the boundary of the domain in a few days (Durán Gómez & Nagai, 2022). Thereafter, the vertically averaged velocity (barotropic velocity $\mathbf{U}_T$) is removed to obtain the baroclinic velocity $\mathbf{u}_T$ corresponding to the M_2 internal tides, that is,

$$\mathbf{u}_T = \widetilde{\mathbf{u}}_T - \mathbf{U}_T = \widetilde{\mathbf{u}}_T - \frac{1}{H}\int_{-H}^{0} \widetilde{\mathbf{u}}_T dz. \tag{3}$$

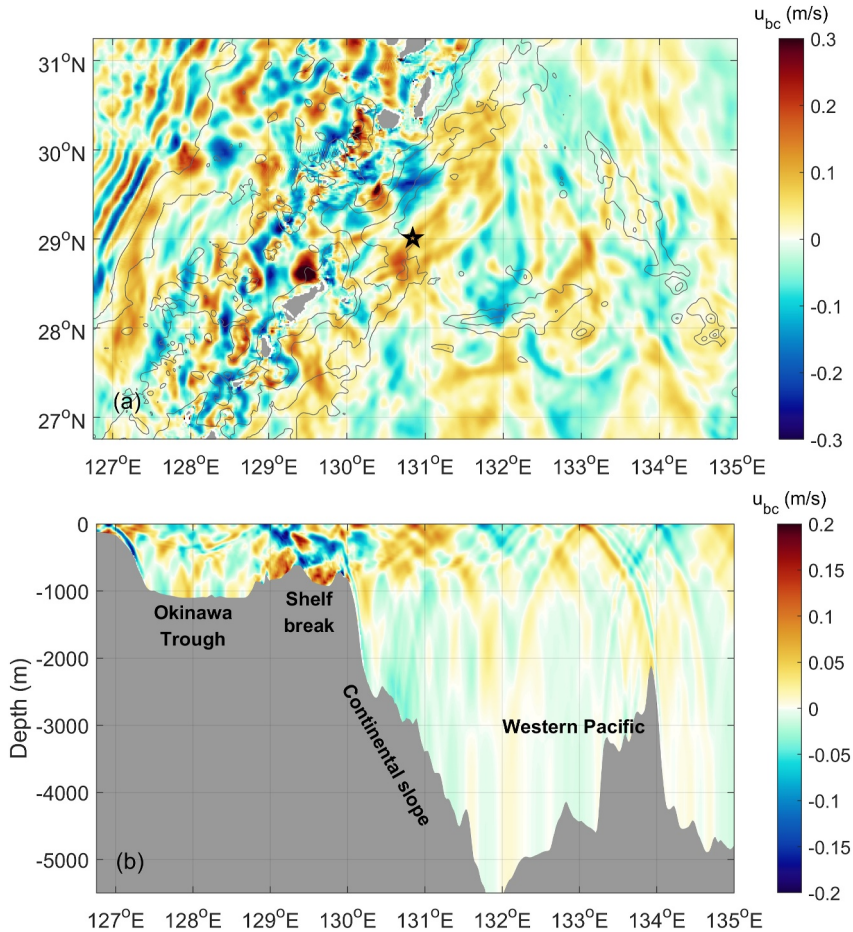

Figure 3. Snapshots of zonal baroclinic velocities (shading) at the end of day 5. (a) For the horizontal plane at $z = -22.5$ m and (b) for the vertical transect along 29°N. In panel (a) gray contours indicate 500, 1,000, 2,000, and 3,000 m isobaths, whereas the black star denotes the location for spectral analysis in Figure 7. Note that the results are from Run-TK.

Figure 3 shows snapshots of zonal baroclinic velocity u_T at the end of day 5 when only the M_2 internal tides are developed. In our study region, the M_2 internal tides are mainly generated at the shelf break between the Yakushima and Amami-oshima Islands, and they propagate in both onshore and offshore directions (Figure 3a). However, the M_2 internal tides radiated into the deep Western Pacific have much larger wavelengths than those going shoreward because internal tides have faster phase speed in the deeper region (Zhao, 2014; Zhao et al., 2016). This feature is also reflected by the vertical transect shown in Figure 3b. In addition, the ray-like structure of the M_2 internal tides is found in the velocity field, indicating the presence of high vertical modes (Niwa & Hibiya, 2004). Moreover, the offshore propagating internal tides from the shelf break interact with those generated at the submarine ridges (134°E), thus giving rise to an interference pattern (Rainville et al., 2010; Wang et al., 2018).

Hereafter, the energetics of the M_2 internal tides are examined. The baroclinic energy flux (**F**) and the barotropic-to-baroclinic energy conversion rate (C) are calculated by the following:

$$\mathbf{F} = \int_{-H}^{0} \left\langle \mathbf{u}_T p_T' \right\rangle dz, \tag{4}$$

and

$$C = -\left\langle (\mathbf{U}_T \cdot \nabla H)\, p_T'(z = -H) \right\rangle, \tag{5}$$

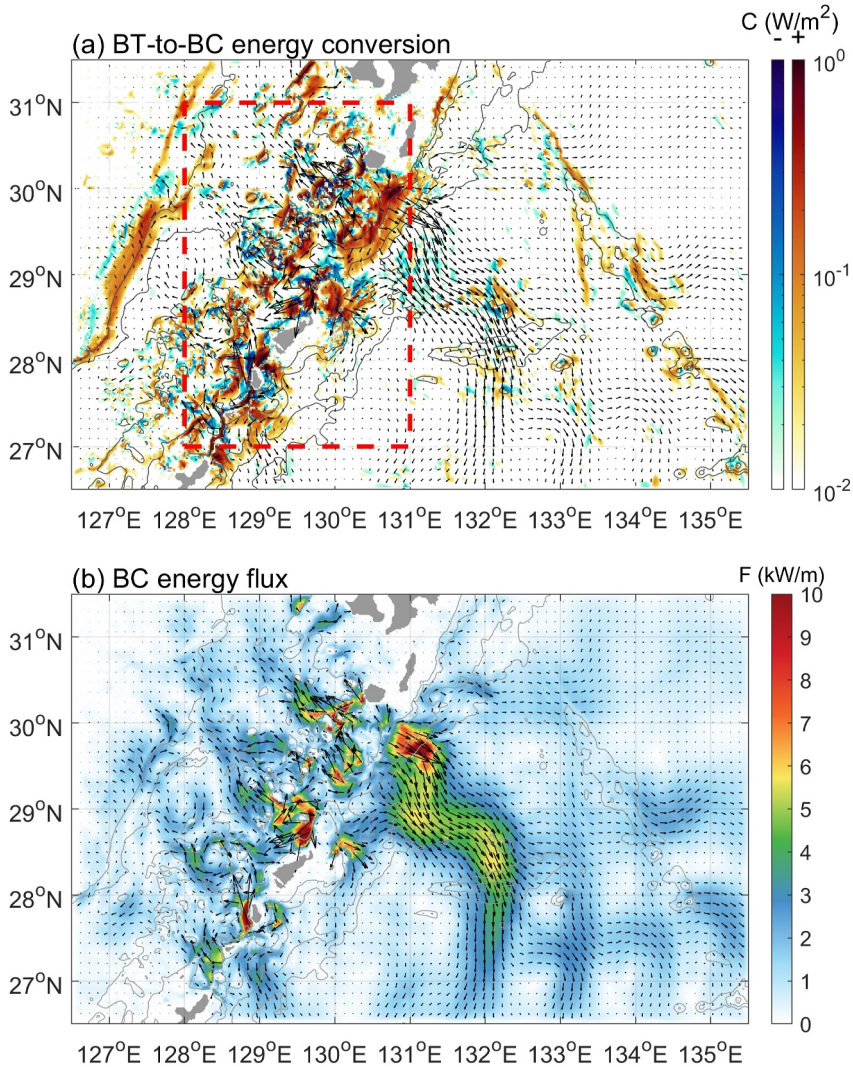

Figure 4. (a) Barotropic-to-baroclinic energy conversion rate (shading, unit: W/m^2). Positive and negative values are indicted by red and blue colors, respectively. The red dashed rectangle indicates the region for integrating the energy conversion. (b) Depth-integrated baroclinic energy flux (shading, unit: kW/m). In each panel, arrows indicate the directions of energy flux, whereas gray contours denote 500, 1,000, 2,000, and 3,000 m isobaths. Note that the results are from Run-TK.

respectively, where <.> denotes the average over a tidal period (Kerry et al., 2013; Nash et al., 2005). In the two equations above, the pressure perturbation corresponding to the M_2 internal tides is obtained by the following:

$$p'_T(z,\,t) = \int_z^0 \rho'_T(\hat{z},\,t)\,g d\hat{z} - \frac{1}{H}\int_{-H}^0\int_z^0 \rho'_T(\hat{z},\,t)\,g d\hat{z}dz, \tag{6}$$

where ρ'_T is the density perturbation induced by the M_2 internal tides from the initial density. As shown in Figure 4a, large energy conversion rates are mainly observed around the shelf break between the Yakushima and Amami-oshima Islands, where the water depth is approximately 500–1,000 m. In addition, weak energy conversion also occurs on the shallow shelf with $H \approx 500$ m west of the Tokara Strait. The area-integrated energy conversion in the Tokara Strait (red dashed rectangle in Figure 4a) is 4.8 GW, generally in accordance with that estimated by Varlamov et al. (2015). Although the presence of the Kuroshio Current causes energy exchange between the M_2 internal tides and background flow, the calculated energy change rates are generally one order of magnitude smaller than C (figure not shown). Southeastward M_2 baroclinic energy fluxes are found near the Tokara Strait, with magnitudes as high as 10 kW/m, which indicates that a large amount of internal tidal energy

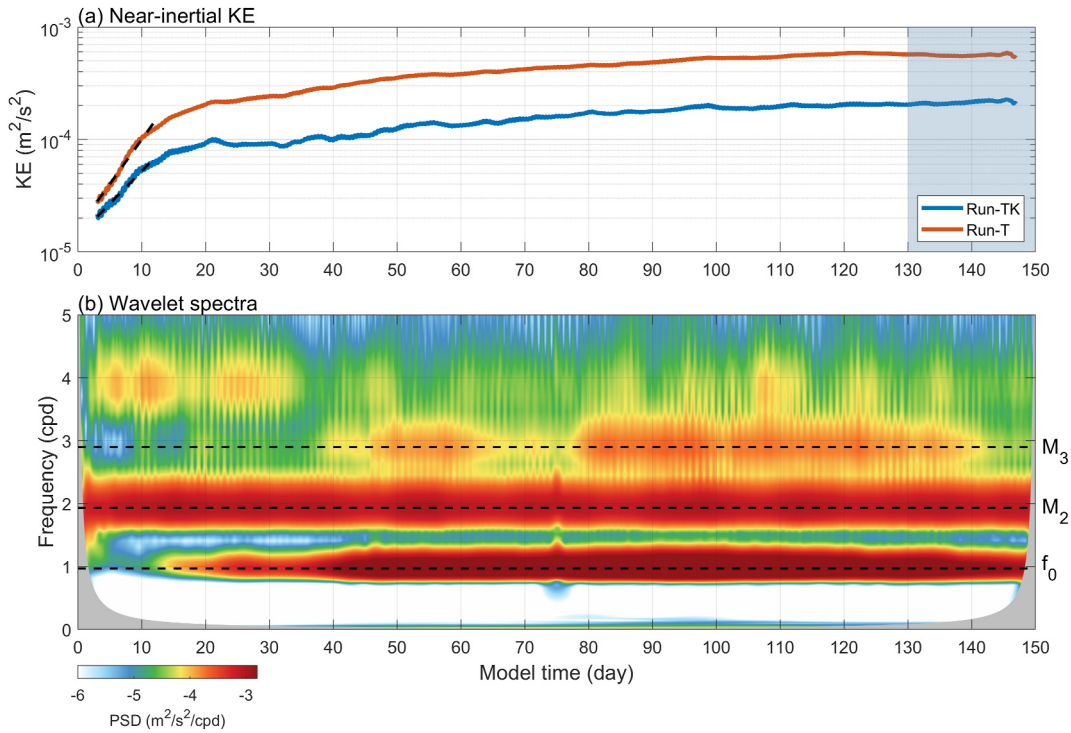

Figure 5. (a) Evolution of domain-averaged near-inertial energy for Run-TK (blue curve) and Run-T (red curve). The growth rates of near-inertial energy are indicated by black dashed lines. The blue shading denotes the steady stage which is considered for analysis. (b) Depth-averaged wavelet spectrum at (131°E, 29°N) for zonal velocity (shading, unit: $m^2/s^2/cpd$) for Run-T. The three black dashed lines indicate the f_0, M_2, and M_3 frequencies.

radiates into the deep Western Pacific (Figure 4b). In addition, narrow beams with smaller energy fluxes in the Okinawa Trough propagate northwestward toward the shallow shelf. These features of the M_2 internal tides in this region are consistent with those reported in previous numerical studies (Niwa & Hibiya, 2004; Varlamov et al., 2015).

3.2. Near-Inertial Waves in Three Runs

Differing from the M_2 internal tides, it takes a much longer time for the near-inertial waves generated via PSI to reach a quasi-steady state in the model (Hazewinkel & Winters, 2011; Liu & Zhao, 2020). To assess the equilibration of near-inertial waves, we filter the near-inertial waves with a frequency band of [0.6 1.4] cpd and calculate the domain-averaged near-inertial kinetic energy (*KE*) for Run-TK and Run-T. The time series of near-inertial *KE* for both runs share a similar feature, even though the near-inertial *KE* in run-TK is lower than that in run-T (Figure 5a). The suppression mechanisms of PSI in the presence of the Kuroshio Current will be considered in Section 4. Here, the near-inertial *KE* grows rapidly in the first 15 days, with the corresponding values increasing by nearly one order of magnitude. Subsequently, the near-inertial *KE* continuously accumulates, but at a slower rate. Finally, a steady state reaches in the last 20 days, during which period the near-inertial energy basically remains invariant. The growth rate of PSI is calculated by linear fitting with the near-inertial *KE* in 3–12 days, which is 0.06 (0.08) day^{-1} for Run-TK (Run-T). Such a time scale (~15 days) is in the same order as the decay time scale of low-mode M_2 internal tides via PSI theoretically predicted by Onuki and Hibiya (2018).

The depth-integrated near-inertial *KE* for the three runs is calculated by using the model results in the last 20 days. As shown in Figures 6a and 6b, the result of run-TK basically shows a similar pattern to that of Run-T, except for the remarkable reduction of near-inertial *KE* in the Okinawa Trough for Run-TK (Figure 6d). Such similarity between Run-TK and Run-T indicates that PSI contributes largely to the generation of near-inertial waves in the study region given that tide is the only energy source in Run-T. Moreover, it should be noted that around the small-scale topographies in the Tokara Strait, near-inertial currents can also be generated due to strong tidal current-topography interaction as suggested by Hibiya et al. (2024). In contrast, although the Kuroshio-

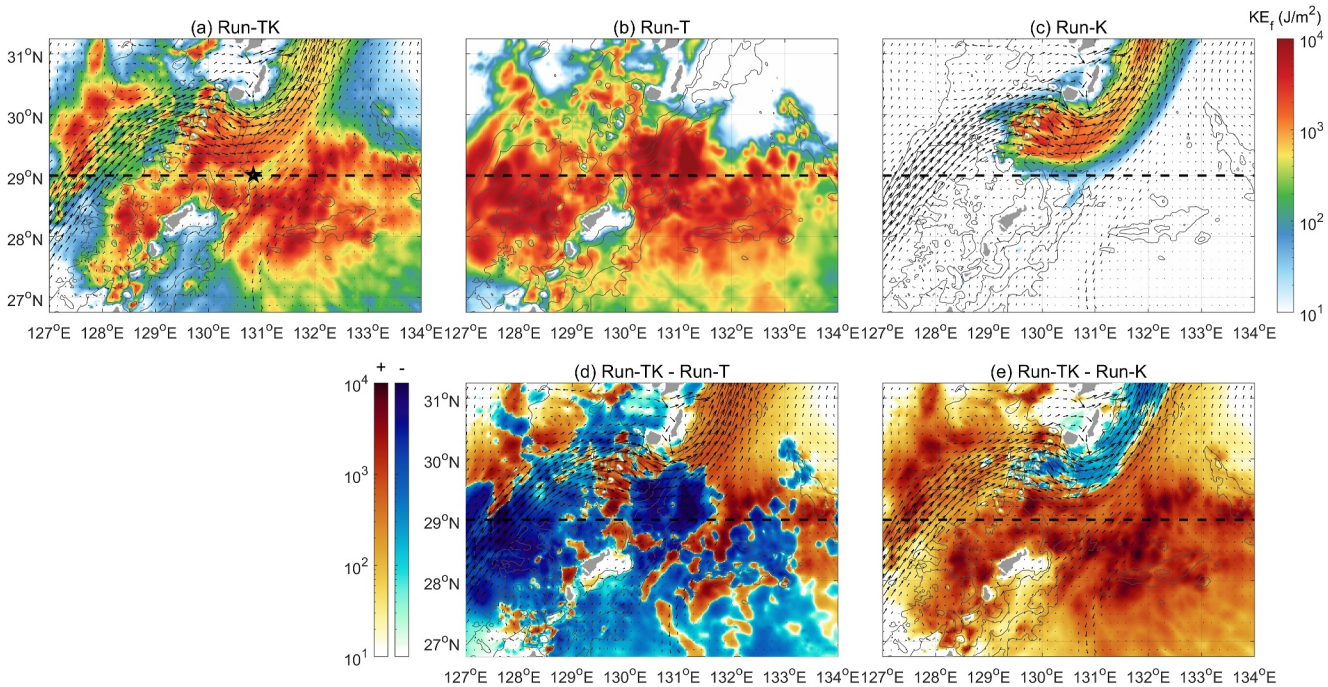

Figure 6. Depth-integrated near-inertial kinetic energy (KE) (log form, shadings, unit: J/m^2) in panels (a) Run-TK, (b) Run-T, and (c) Run-K. Differences in depth-integrated near-inertial KE (log form, shadings, unit: J/m^2) (d) between Run-TK and Run-T and (e) between Run-TK and Run-K. The positive (negative) values indicate that the near-inertial KE in Run-TK is higher (lower) than that in Run-K. Gray contours in each panel denote 500, 1,000, 2,000, and 3,000 m isobaths, whereas arrows in panels (a), (c), and (d) indicate the background current.

Topography interaction also gives rise to near-inertial waves (Nagai et al., 2021), these waves are restricted within the Kuroshio Current downstream from the Tokara Strait (Run-K, Figure 6c); outside the Kuroshio region, the near-inertial *KE* remains at a low level. Furthermore, by calculating the difference in near-inertial *KE* for Run-TK and Run-K, it is easy to find that including tidal forcing in the model significantly elevates the near-inertial *KE* in most of the area of the model domain, except for the region within the Kuroshio Current downstream the Tokara Strait where the near-inertial energy somewhat decreases (Figure 6e). These results highlight the significant role of PSI in generating near-inertial waves in this region, even in the presence of the Kuroshio Current. Next, a detailed analysis of PSI is conducted for Run-TK, which takes into account the realistic conditions of the Tokara Strait.

3.3. PSI of the M_2 Internal Tides: Characteristics (Run-TK)

Figure 7a shows the depth-averaged power spectra of the baroclinic velocities at the M_2 critical latitude (130.84°E, 29°N). During the first 10 days, a dominant peak at the M_2 tidal frequency is found. Meanwhile, small peaks at the M_4 are detected, indicating the generation of higher harmonics of the M_2 internal tides. In contrast, during the last 10 days, a remarkable peak appears at the local inertial frequency. Its spectral value is increased by one order of magnitude when compared with that in the first 10 days. In addition, a lower peak at the M_3 tidal frequency is also identified, which is absent in the result for the first 10 days. Because the M_3 tidal frequency is the sum of the M_2 tidal frequency and the local inertial frequency, it is considered to be excited via the nonlinear interaction between the M_2 internal tides and PSI-generated near-inertial waves. This will be further discussed in Section 5.

The occurrence of PSI is evidenced by calculating the vertical wavenumber spectrum of baroclinic velocities from which the vertical scales of near-inertial waves can be examined (e.g., Richet et al., 2018; Wang, Cao, Liang, et al., 2021). Before the calculation, Wentzel-Kramers-Brillouin–Jeffreys (WKBJ) stretching is applied to depth $\left(z_{wkb} = \int_z^0 N(z)/N_0 dz\right)$ and velocity $\left(u_{wkb} = u\sqrt{N_0/N(z)}\right)$ to account for the variation of stratification along the vertical direction and a reference buoyancy frequency $N_0 = 5.2 \times 10^{-3}$ s^{-1} is used (Nelson et al., 2020). In the spectra, the negative (positive) wavenumbers correspond to the upward (downward) radiation of energy. During

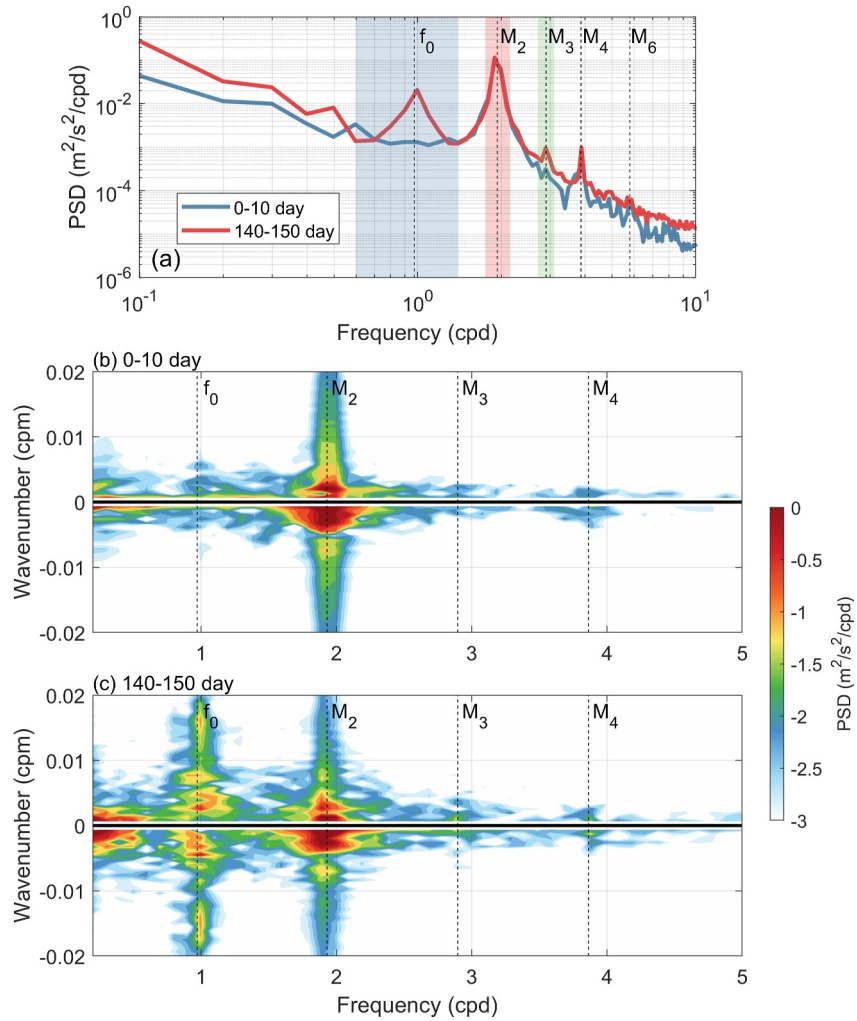

Figure 7. (a) Power spectra for zonal baroclinic velocity in the first and last 10 days at (130.84°E, 29°N). Blue and red shadings indicate the near-inertial and semidiurnal bands, respectively. Vertical wavenumber-frequency spectra (shading, unit: m^2/s^2/cpd) in the (b) first and (c) last 10 days. Note that WKBJ stretched velocities are used before the calculation of wavenumber-frequency spectra. The results are from Run-TK.

the first 10 days, the M_2 internal tides are dominant (Figure 7b). Large spectral densities at the M_2 tidal frequency are located in the lower half plane, suggesting the upward propagation of internal tides at this location. In addition, most of these values correspond to a vertical wavenumber smaller than 0.005 cpm. On the other hand, the spectrum for the results in the last 10 days shows an apparently different pattern (Figure 7c). Remarkable spectral densities appear around the local inertial frequency. In a wavenumber range of 0.01–0.02 cpm, the spectral densities of near-inertial signals are larger than those around the M_2 tidal frequency, suggesting that the near-inertial waves have smaller vertical scales than the M_2 internal tides. These near-inertial waves propagate both upward and downward to form a resonant triad according to Equation 2 (McComas & Bretherton, 1977). Additionally, the upward and downward waves have comparable intensities as inferred from the spectrum, which has been illustrated by oceanic observations near the critical latitude (Girton et al., 2011; MacKinnon, Alford, Pinkel, et al., 2013). Moreover, a bispectral analysis is performed, whose results provide further evidence of the occurrence of PSI (see Supporting Information S1).

Figures 8a and 8b show the depth-time map of filtered zonal velocities for the M_2 internal tides and near-inertial waves. The former exhibits a low-mode pattern, whereas the latter is largely contributed by high modes, since the near-inertial velocities change their signs several locations in the vertical direction. The near-inertial velocities are

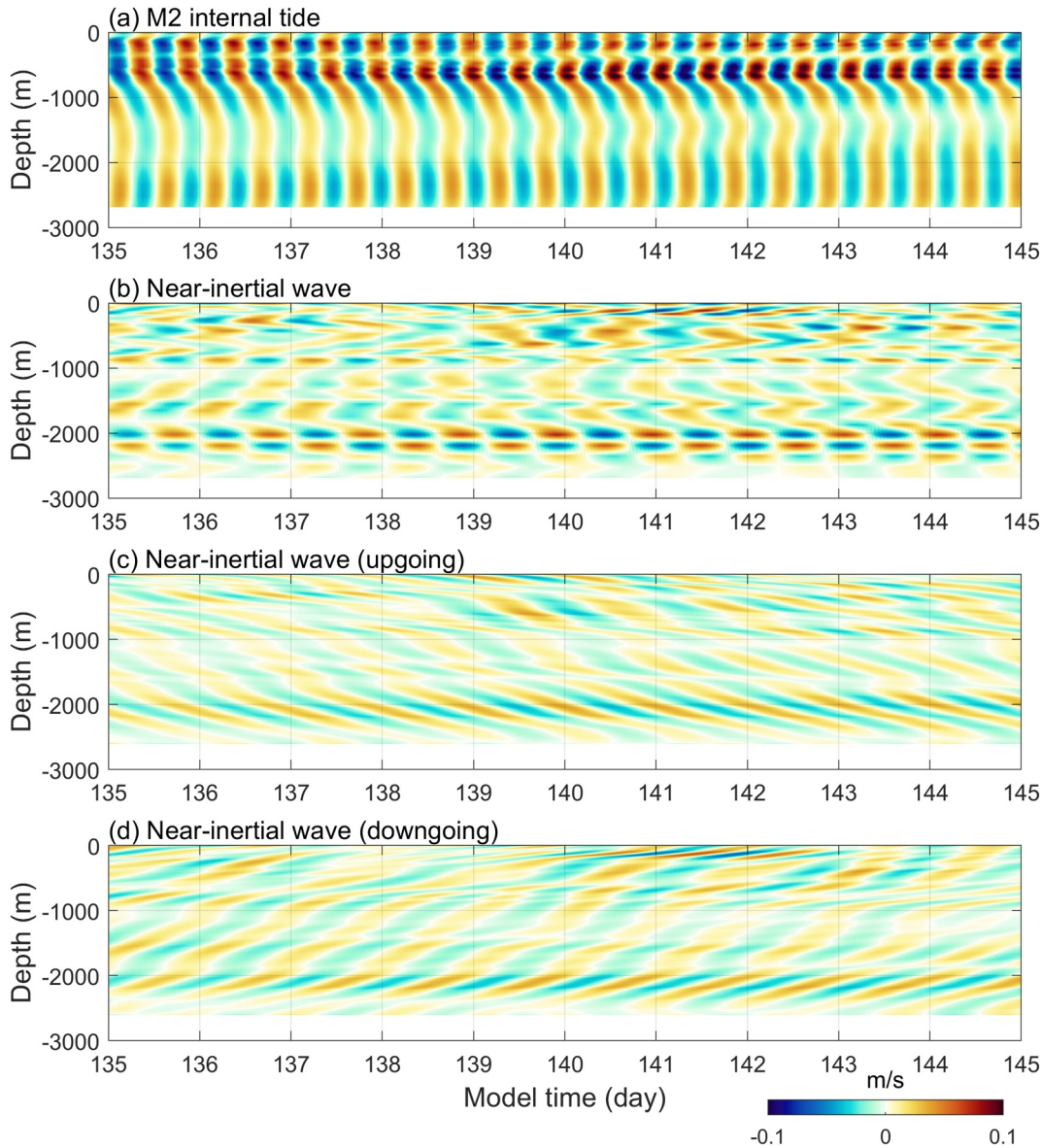

Figure 8. Depth-time map for (a) semidiurnal (b) near-inertial zonal baroclinic velocities (shadings, unit: m/s) at (130.84°E, 29°N). Upgoing and downgoing components of near-inertial waves are shown in panels (c) and (d) respectively. Here, "upgoing" and "downgoing" indicate the propagation direction of energy. Note that the results are from Run-TK.

further decomposed into upgoing and downgoing components. The two components are comparable in strength (Figures 8c and 8d), consistent with the spectral analysis (Figure 7c).

Then attention is paid to the spatial structure and propagation of near-inertial waves induced by PSI. As shown in Figures 9a and 9d, the near-inertial waves are generated at the shelf break within 28–30°N. Because PSI is not fully developed at that time, these near-inertial waves may be attributed to both PSI and Kuroshio-Topography interaction. With the growth of PSI, the near-inertial waves are strengthened. These waves propagate downstream with the Kuroshio Current. During this stage, large near-inertial velocities are limited in the upper ocean at depths shallower than 500 m, and no signal of near-inertial waves appears in the deep ocean (Figures 9b and 9e).

When the near-inertial waves are fully developed, large near-inertial velocities are found not only in the Tokara Strait but also on the shallow shelf northwest of the Okinawa Trough (Figure 9c), whereas the near-inertial waves are absent in the Okinawa Trough. Most of the generated near-inertial waves propagate downstream with the Kuroshio Current; whereas only a small fraction of them radiates southeastward into the Pacific Ocean as

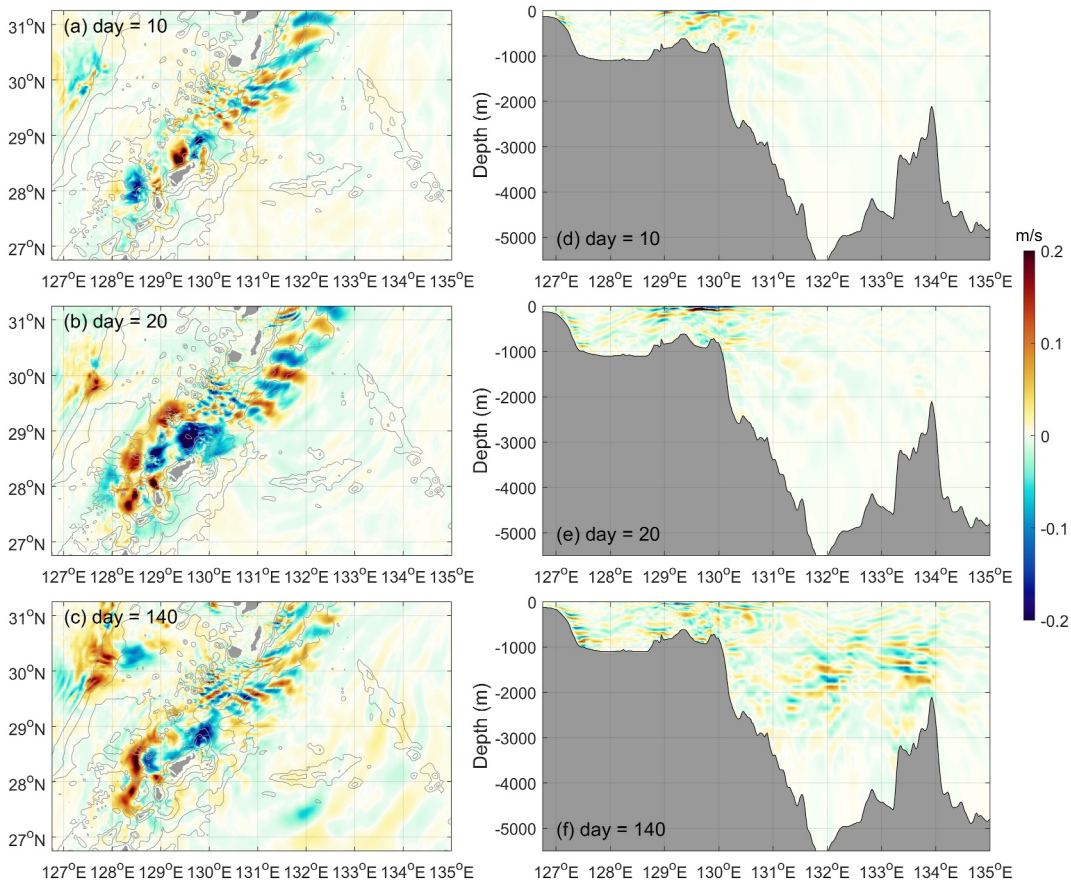

Figure 9. (a–c) Snapshots of zonal baroclinic velocities for near-inertial waves (shading, unit: m/s) at $z = -22.5$ m. (d–f) Same as (a–c) but in the vertical transect along 29°N. Gray contours in panels (a–c) denote 500, 1,000, 2,000, and 3,000 m isobaths. Note that the results are from Run-TK.

indicated by week near-inertial velocity here. In the vertical transect, high-wavenumber signals of near-inertial waves are seen, which shows a horizontally layered structure (Figure 9f). A similar structure of PSI-generated near-inertial waves has been revealed in both the ideal (MacKinnon & Winters, 2005) and realistic numerical simulations (Ansong et al., 2018; Simmons, 2008). The slopes of these baroclinic velocity layers are nearly zero, agreeing with that of the theoretical raypath for near-inertial waves (Nagai et al., 2017). In the deep Western Pacific east of 131°E, intense near-inertial velocities are mainly found within 500–3,000 m rather than in the upper ocean (Figure 9f).

3.4. PSI of the M_2 Internal Tides: Energetics (Run-TK)

Next, we focus on the energetics of PSI-generated near-inertial waves. The energy equation for the near-inertial waves (i.e., the subharmonic waves) is given below:

$$\overline{\frac{\partial}{\partial t}\left(KE_f + APE_f\right)} + \nabla \cdot \overline{\mathbf{F}_f} = \overline{G} + \overline{g_f} - \overline{D_f} \tag{7}$$

whose derivation can be found in Supporting Information S1. The overbar in each term denotes a time average. The terms in Equation 7 are baroclinic KE KE_f, available potential energy APE_f, energy flux $\mathbf{F}_f$, PSI energy transfer rate G, wave-current energy exchange rate g_f, and dissipation rate D_f, which are calculated by (Nagai et al., 2015; Onuki & Hibiya, 2015)

$$KE_f = \frac{1}{2}\rho_0\left(u_f^2 + v_f^2\right) \tag{8}$$

$$APE_f = \frac{g^2 \rho_f'^2}{2\rho_0 N^2} \tag{9}$$

$$\mathbf{F}_f = \mathbf{u}_f p_f' + (\mathbf{U} + \mathbf{u}_T)\left(KE_f + APE_f\right) \tag{10}$$

$$G = -\rho_0\left(u_f u_f \frac{\partial u_T}{\partial x} + u_f v_f \frac{\partial u_T}{\partial y} + v_f u_f \frac{\partial v_T}{\partial x} + v_f v_f \frac{\partial v_T}{\partial y}\right) \tag{11}$$

$$g_f = -\rho_0\left(u_f u_f \frac{\partial U}{\partial x} + u_f v_f \frac{\partial U}{\partial y} + v_f u_f \frac{\partial V}{\partial x} + v_f v_f \frac{\partial V}{\partial y}\right) \tag{12}$$

$$D_f = \rho_0 A_H\left[\left(\frac{\partial u_f}{\partial x}\right)^2 + \left(\frac{\partial u_f}{\partial y}\right)^2 + \left(\frac{\partial v_f}{\partial x}\right)^2 + \left(\frac{\partial v_f}{\partial y}\right)^2\right] + \rho_0 A_V\left[\left(\frac{\partial u_f}{\partial z}\right)^2 + \left(\frac{\partial v_f}{\partial z}\right)^2\right] \tag{13}$$

The subscripts T and f denote the M_2 internal tides and near-inertial waves, respectively; and $\mathbf{U}$ is the background current. According to the order estimation by Onuki and Hibiya (2015), the buoyancy and vertical shear production terms in G can be neglected because of the insignificant vertical displacement of near-inertial waves, so Equation 11 has been widely used in previous studies (e.g., Ansong et al., 2018; MacKinnon & Winters, 2005; Wang, Cao, Chen, et al., 2021, Wang, Cao, Liang, et al., 2021). Moreover, the internal tidal KE and dissipation rate are calculated as follows:

$$KE_T = \frac{1}{2}\rho_0\left(u_T^2 + v_T^2\right) \tag{14}$$

and

$$D_T = \rho_0 A_H\left[\left(\frac{\partial u_T}{\partial x}\right)^2 + \left(\frac{\partial u_T}{\partial y}\right)^2 + \left(\frac{\partial v_T}{\partial x}\right)^2 + \left(\frac{\partial v_T}{\partial y}\right)^2\right] + \rho_0 A_V\left[\left(\frac{\partial u_T}{\partial z}\right)^2 + \left(\frac{\partial v_T}{\partial z}\right)^2\right] \tag{15}$$

Here, the velocities corresponding to the M_2 internal tides and near-inertial waves are extracted with the fourth-order Butterworth filter as described above. We use the model results in the last 20 days in the calculations, when both the internal tides and near-inertial waves reach an equilibration state.

Figures 10a and 10b show the distributions of depth-integrated baroclinic *KE* for the M_2 internal tides and near-inertial waves, respectively. Large baroclinic *KE* for the M_2 internal tides mainly appears at the shelf break between the Yakushima and Amami-oshima Islands where high energy conversion rates are found (Figure 10a). As the M_2 internal tides propagate southeastward into the Western Pacific and northwestward into the Okinawa Trough, their *KE* gradually decays. However, the result for near-inertial waves exhibits different features (Figure 10b). First, the near-inertial *KE* is restricted within the region south of 30°N, particularly in the deep Western Pacific. Second, there is a lack of near-inertial *KE* in the Okinawa Trough where high internal tidal *KE* exists. Moreover, near-inertial *KE* is enhanced downstream of the Kuroshio Current from the islands in the central region of the Tokara Strait (around 129.5°E, 29.5°N). By calculating the zonally averaged *KE*, we find that the near-inertial waves are latitude-dependent (Figure 10c). Namely, near-inertial *KE* is high around the M_2 critical latitude. With the increase of distance from the M_2 critical latitude, the near-inertial *KE* decreases quickly. At 27°N and 31°N, the near-inertial *KE* is approximately one order of magnitude lower than that at around the critical latitude. In contrast, the M_2 internal tidal *KE* in this region is much less dependent on the latitude.

Previous studies have indicated that the Tokara Strait is an energy sink for internal tides (Niwa & Hibiya, 2004; Tsutsumi et al., 2017; Varlamov et al., 2015). As shown in Figure 10d, two regions with high energy dissipation rates of the M_2 internal tides are identified, that is, the continental shelf break between the Yakushima and Amami-oshima Islands and the shallow East China Sea shelf ($H < 500$ m). The former is due to the local dissipation of internal tides, whereas the latter may be attributed to the dissipation of shoaling internal tides. In the

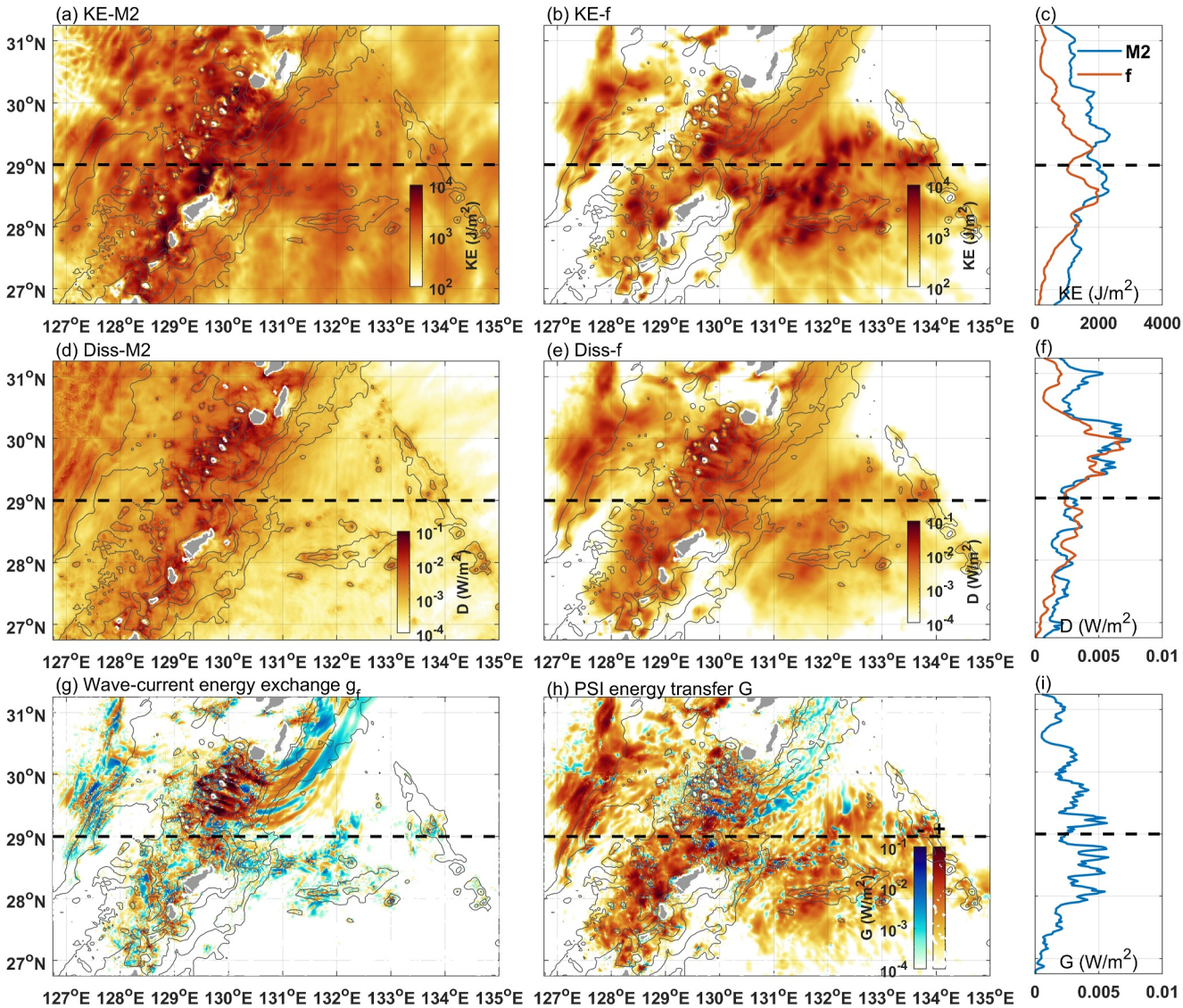

Figure 10. Depth-integrated kinetic energy for (a) the M_2 internal tides and (b) near-inertial waves (log form, shadings, unit: J/m^2). Corresponding zonal-averaged values (127–133°E) are shown in panel (c). (d)–(f) Same as (a)–(c) but for energy dissipation (log form, shadings, unit: W/m^2). Depth-integrated (g) near-inertial wave-current energy exchange and (h) parametric subharmonic instability (PSI) energy transfer rates (shadings, unit: W/m^2). Positive and negative values in panels (g) and (h) are indicted by red and blue colors, respectively. (i) Zonal-averaged (127–133°E) PSI energy transfer rate. In each panel, the M_2 critical latitude is denoted by the black dashed line. Gray contours in panels (a), (b), (d), (e), (g), and (h) denote 500, 1,000, 2,000, and 3,000 m isobaths. Note that the results are from Run-TK.

Western Pacific, the M_2 internal tidal dissipation rates are approximately 1–2 orders of magnitude lower than those around the shelf break. As for the energy dissipation rates of near-inertial waves, they show a similar pattern to that of the near-inertial *KE* (Figure 10e). Although the near-inertial waves are weaker than the M_2 internal tides, the energy dissipation rates they induced are comparable to or even higher than those of internal tides, particularly in the region southwest of the Yakushima Island and Western Pacific southeast of the Tokara Strait. This is further illustrated by the zonally averaged result shown in Figure 10f. Differing from the *KE*, energy dissipation rates of near-inertial waves are enhanced around 30°N, corresponding to the latitude at which several islands and seamounts are located in the Tokara Strait.

The depth-integrated energy transfer rate is shown in Figure 10h. Nearly all the values of *G* are positive, indicating that the energy is transferred from the internal tides to subharmonic waves. There are two regions with a large value of *G*: one is around the Amami-oshima Island in the southern part of the Tokara Strait; whereas the other is located on the shallow shelf northwest of the Okinawa Trough. This result suggests that energy transfer

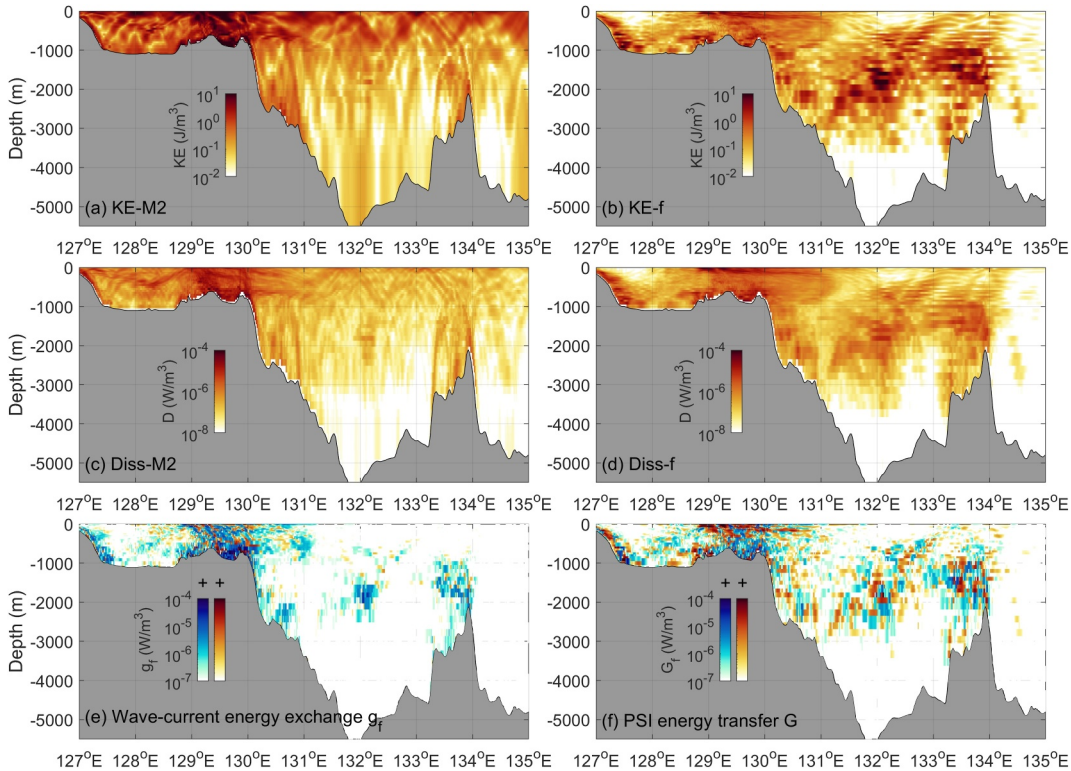

Figure 11. Baroclinic kinetic energy (log form, shadings, unit: J/m^3) for (a) the M_2 internal tides and (b) near-inertial waves along 29°N. (c)–(d) Same as (a) and (b) but for energy dissipation rate (log form, shadings, unit: W/m^3). (e) Near-inertial wave-current energy exchange and (f) Parametric subharmonic instability energy transfer rates along 29°N (shading, unit: W/m^3). Positive and negative values in panels (e) and (f) are indicted by red and blue colors, respectively. Note that the results are from Run-TK.

via PSI occurs locally (Wang, Cao, Chen, et al., 2021, Wang, Cao, Liang, et al., 2021). In contrast, G remains at relatively low level in most regions of the deep Western Pacific. Additionally, the energy transfer rate basically shows a similar pattern to energy dissipation rates of near-inertial waves (Figures 10e and 10h), which implies that the energy balance for the PSI-generated near-inertial waves is largely dominated by energy transfer G and dissipation terms D_f in Equation 7. In other words, a large amount of energy transferred to the near-inertial waves via PSI is dissipated locally instead of being radiated away from the topography. Intensification of energy transfer around the M_2 critical latitude is also found in the zonally averaged results (Figure 10i). Moreover, some negative values of G are found within the Kuroshio Current downstream from the Tokara Strait. This may result from the interaction between the M_2 internal tides and near-inertial waves excited through Kuroshio-Topography interaction because the latter do not necessarily have a phase correlation with the former (Yang et al., 2020).

In addition to PSI, near-inertial waves also gain energy from the Kuroshio Current, since positive wave-current energy transfer rates are found near several small islands and seamounts in the Tokara Strait (Figure 10g). This is because the Kuroshio-Topography interaction excites near-inertial waves downstream from the topography (Figure 6c). Moreover, PSI-generated near-inertial waves may interact with the Kuroshio Current, which leads to the energy exchange. Given that the two above processes are complicatedly intertwined, we cannot separate their contributions to the energy change rate. Moreover, note that g_f in the Tokara Strait is comparable to the PSI energy transfer rate (Figure 10h), implying that the wave-mean flow interaction can also have a considerable effect on the energy budget of near-inertial waves.

Figure 11 shows the vertical structure of the variables presented in Figure 10 at the M_2 critical latitude. For the M_2 internal tides, both KE and D are intensified in the upper 1,000 m (Figures 11a and 11c). In addition, the energy dissipation in the deep layers of the Western Pacific Ocean is weaker than that near the shelf break (generation sites) Figure 11c. On the other hand, near-inertial waves behave differently from the M_2 internal tides, especially in the Western Pacific. In the east of the steep continental slope, high KE and D of near-inertial waves are found

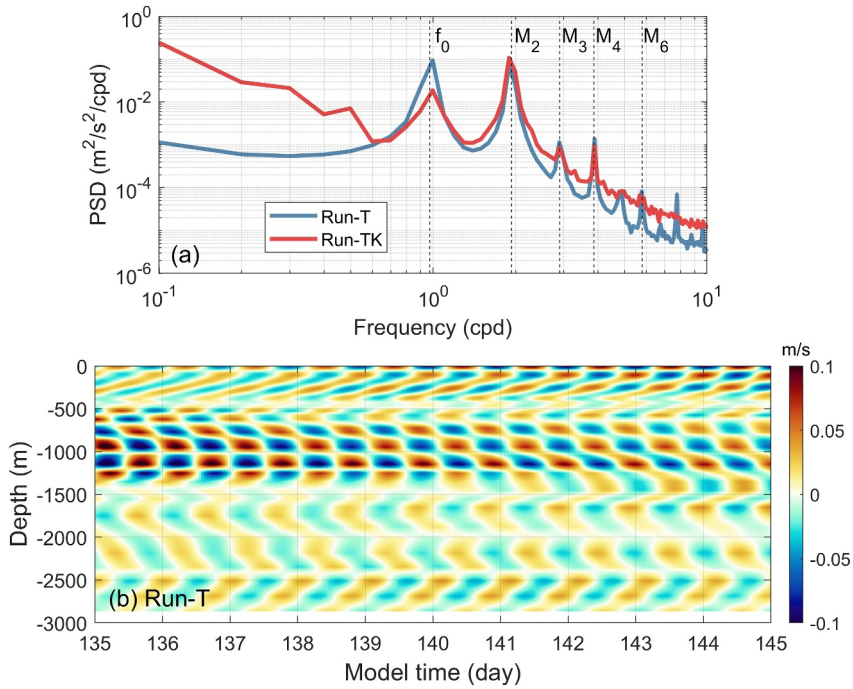

Figure 12. (a) Depth-averaged power spectra of zonal baroclinic velocities in the last 10 days at (130.84°E, 29°N). Results with (Run-TK) and without background currents (Run-T) are denoted by red and blue curves, respectively. (b) Filtered near-inertial velocities for Run-T (shading, unit: m/s).

below 500 m. In this region, dissipation rates of near-inertial waves are approximately one order of magnitude higher than those of the M_2 internal tides. This implies that the PSI-generated near-inertial waves also considerably influence the mixing in the deep water. Around the shelf break, energy dissipation rates of near-inertial waves are approximately of the same order of magnitude as those of the M_2 internal tides, but they are elevated in the near-surface layer.

Energy transfer via PSI mainly occurs locally around the generation sites of internal tides. Correspondingly, in addition to the shelf break, high positive energy transfer rates are also found over the ridge crest at 134°E and the slope west of the Okinawa Trough (Figure 11f). In other regions far from the generation sites, large energy transfer rates are absent because low internal tidal energy is unfavorable for the growth of PSI (Nikurashin & Legg, 2011; Simmons, 2008; Wang, Cao, Chen, et al., 2021). The calculated energy transfer rates around the Tokara Strait are slightly higher but comparable to those estimated by Ansong et al. (2018) based on a global ocean circulation model, and are at a similar magnitude to those observed at the north of the Hawaii Islands (MacKinnon, Alford, Sun, et al., 2013) or equatorward of the M_2 critical latitude of Mien-Hua Canyon northeast of the Taiwan Island (Yang et al., 2020). The wave-current energy exchange rates are remarkable only around the Tokara Strait, consistent with the above results (Figure 11e).

4. Influence of the Kuroshio Current on PSI

4.1. Results

To clarify the influence of Kuroshio Current on PSI of the M_2 internal tides in the Tokara Strait, we compare the power spectra of baroclinic velocities from Run-T and Run-TK (Figure 12a). The peak at the local near-inertial frequency for Run-T is much higher than that for Run-TK, suggesting that PSI is suppressed in the presence of the Kuroshio Current at this location. The filtered high-wavenumber near-inertial velocities for Run-T are apparently stronger than those shown in Figure 8b, especially within a depth of 500–1,500 m where the "checkerboard" pattern is found (Figure 12b).

We also calculate the KE and dissipation rate of near-inertial waves as well as the energy transfer rate for Run-T using the method described in Section 3.3 (Figures 13 and 14). By comparing the results of Run-TK and Run-T,

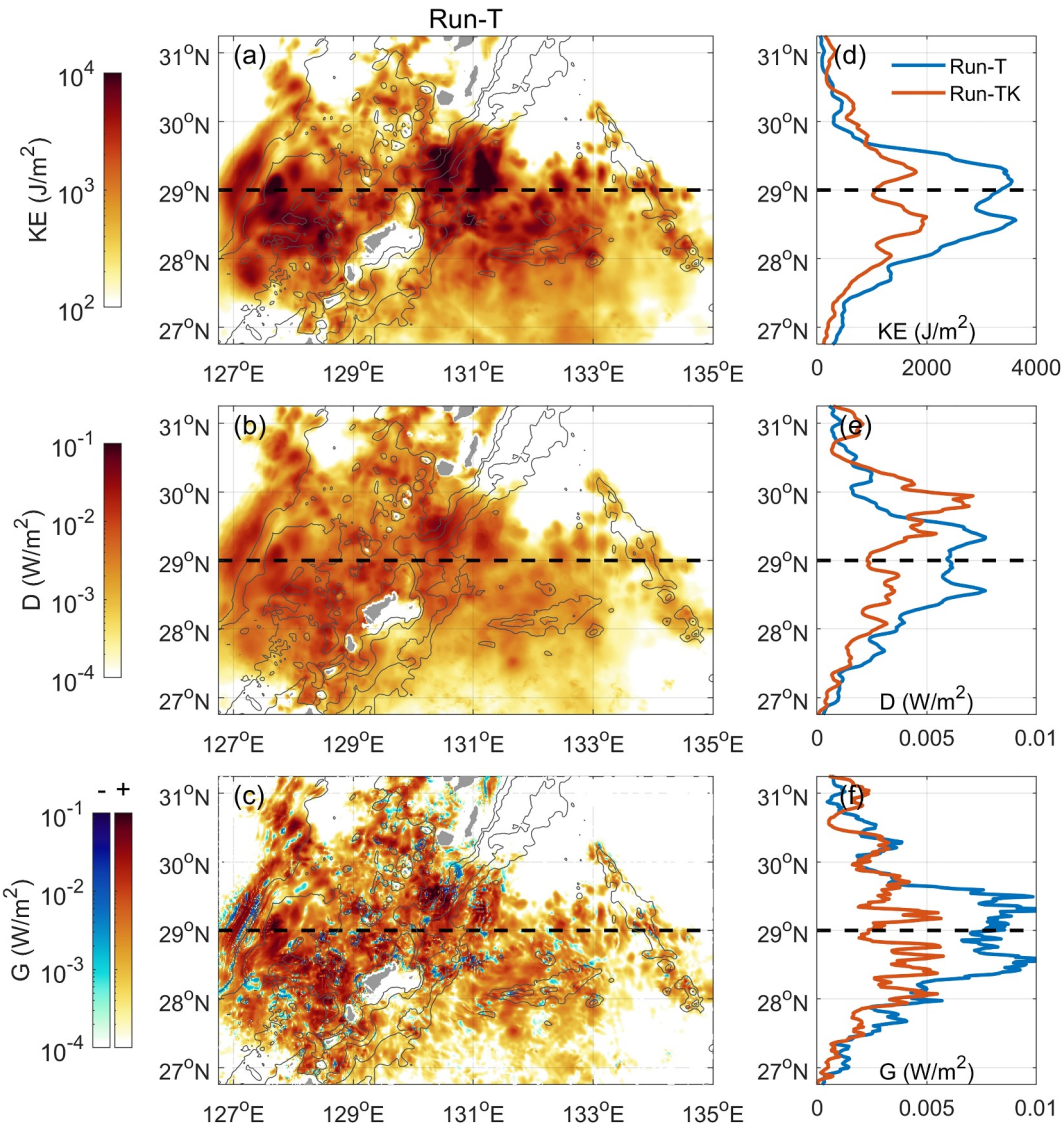

Figure 13. Depth-integrated (a) near-inertial baroclinic kinetic energy (log form, shading, unit: J/m^2), (b) energy dissipation rate (log form, shading, unit: W/m^2), and (c) PSI energy transfer rate (shading, unit: W/m^2) for Run-T. Corresponding zonally averaged results are shown in panels (d), (e), and (f), respectively (blue curves). The results of Run-TK are also plotted for comparison (red curves). Gray contours in panels (a), (b), and (c) show 500, 1,000, 2,000, and 3,000 m isobaths; whereas the black dashed line in each panel denotes the M_2 critical latitude.

we find that the Kuroshio Current significantly modulates the energetics of PSI in this region. As shown in Figures 13a and 13b, both the near-inertial *KE* and dissipation are obviously elevated in the Okinawa Trough in the absence of the Kuroshio Current. These phenomena are also reflected by the results along the 29°N transect that large *KE* and *D* of near-inertial waves distribute throughout the whole water column in the Okinawa Trough in Run-T (Figures 14a–14c). Consequently, *KE* and *D* of near-inertial waves are remarkably peaked at the critical latitude (Figures 13d and 13e), whereas they change little in magnitudes in other regions with weak background currents (e.g., the shelf break around the Amami-oshima Island and the shallow shelf northwest of the Okinawa Trough).

The Kuroshio Current also inhibits the energy transfer from the M_2 internal tides to the near-inertial waves via PSI, especially in the Okinawa Trough and southwest of Yakushima Island (Figure 13c). It is indicated by the difference in depth-integrated energy transfer rates between Run-TK and Run-T (See Supporting Information S1). Additionally, the zonally averaged energy transfer rates for Run-T are almost twice larger than those for Run-TK

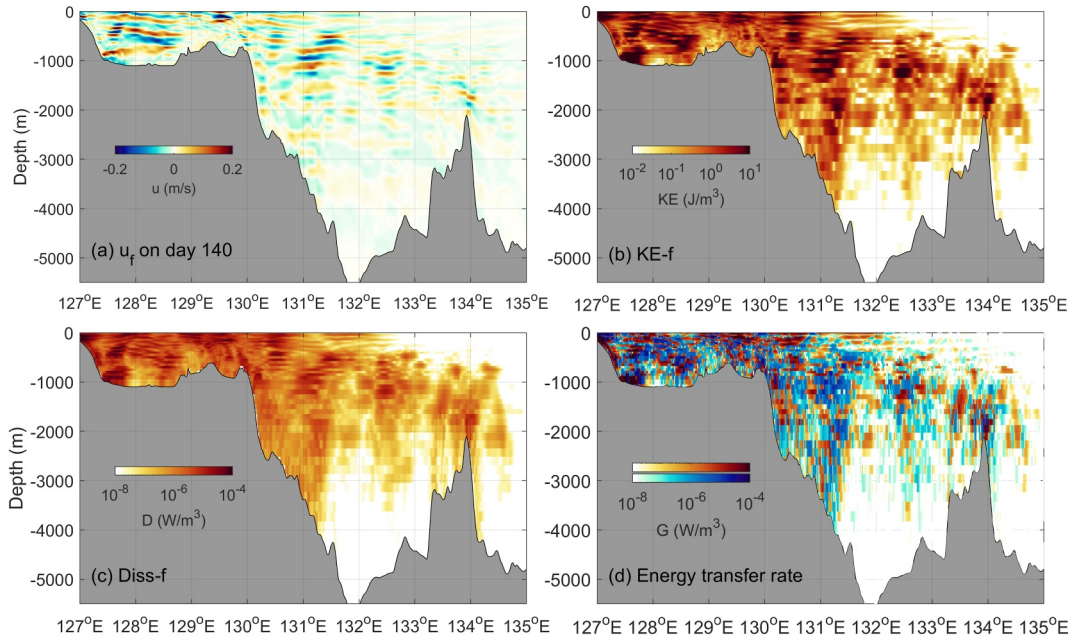

Figure 14. Vertical transects along 29°N for (a) snapshots of near-inertial velocity on day 140 (shading, unit: m/s), (b) near-inertial kinetic energy (log form, shading, unit: J/m^3), (c) energy dissipation rate (log form, shading, unit: W/m^3), and (d) energy transfer rate (shading, unit: W/m^3) without background currents (Run-T).

at the critical latitude, with the appearance of a remarkable peak (Figure 13f). Based on the above results, it can be concluded that the Kuroshio Current suppresses PSI of the M_2 internal tides in our study region.

4.2. Mechanisms

Then, we pay attention to the mechanism by which the Kuroshio Current suppresses PSI of internal tides in the Tokara Strait and Okinawa Though. The PSI growth is determined by the energy of the parent waves, that is, the internal tides (Nikurashin & Legg, 2011; Simmons, 2008; Wang, Cao, Chen, et al., 2021). Namely, weak internal tides are unfavorable for the development of PSI. Hence, we conjecture that the Kuroshio Current may influence PSI by affecting the generation of internal tides in the Tokara Strait. However, the integrated energy conversion of the M_2 internal tides in the Tokara Strait for Run-T even decreases by 8% compared to that for Run-TK. Therefore, this mechanism can be ruled out.

Previous studies indicate that PSI can be modulated by background currents (Wang, Cao, Liang, et al., 2021; Yang et al., 2018), as they change the minimum frequency of internal waves:

$$\omega_{\min} = f_0\sqrt{1 + Ro - Ri^{-1}}, \tag{16}$$

where $Ro = (V_x - U_y)/f_0$ and $Ri = N^2/\left(U_z^2 + V_z^2\right)$ are the Rossby and Richardson numbers of background currents, respectively (Schlosser et al., 2019; Thomas & Taylor, 2014; Whitt & Thomas, 2013). In this situation, efficient PSI would occur only in the region where $\omega_{\min} = \omega_0/2$.

We calculate $\omega_{\min}$ by using the time-averaged velocity field from the Run-TK and then normalize it by $\omega_0/2$. As shown in Figure 15, the presence of the Kuroshio Current causes a complex spatial pattern of the $\omega_{\min}$. Generally, on the left (right) side of the axis of the Kuroshio Current, positive (negative) relative vorticity is dominant, resulting in the increase (decrease) of the $\omega_{\min}$, which is also reflected in the vertical transect shown in Figure 15b. In addition, as the Kuroshio Current interacts with small islands southwest of Yakushima Island, alternative bands of strong vorticity are found in the island wake (Liu et al., 2019). As a result, both the near-inertial *KE* and energy transfer rates via PSI are weakened (Figure 13). In contrast, in the regions with weak background currents (the shelf break around the Amami-oshima Island and shallow shelf northwest of the Okinawa Trough), efficient PSI

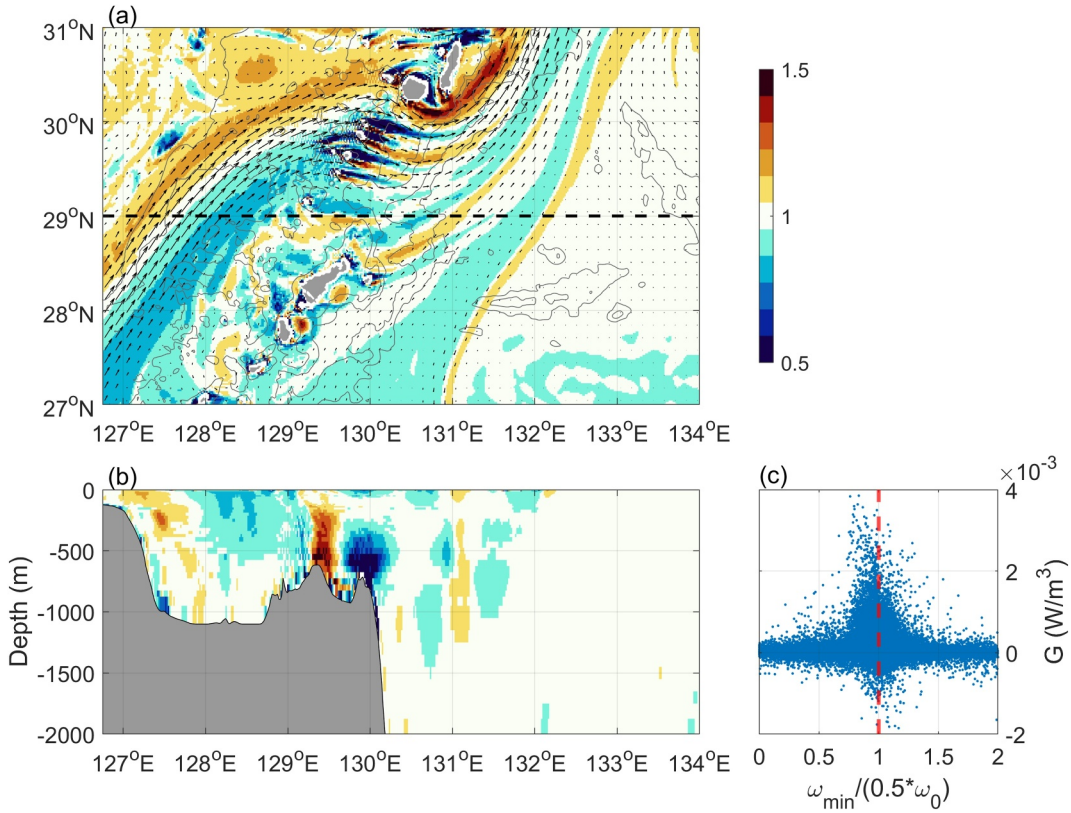

Figure 15. Minimum wave frequency (a) at $z = -22.5$ m and (b) along 29°N normalized by $\omega_0/2$ (shadings). In panel (a), the black dashed line indicates the M_2 critical latitude, and gray contours denote 500, 1,000, 2,000, and 3,000 m isobaths. (c) Parametric subharmonic instability energy transfer rate within 127–134°E as a function of normalized minimum wave frequency. The red dashed line indicates $\omega_{\min} = \omega_0/2$.

still occurs, as evidenced by the high near-inertial energy and dissipation rates (Figures 10b and 10e). The modulation of the minimal wave frequency for PSI is further confirmed by the scatterplot of normalized $\omega_{\min}$ and PSI energy transfer rate (Figure 15c). It is easy to find high values of G when $\omega_{\min} = \omega_0/2$. When $\omega_{\min}$ is higher or lower than $\omega_0/2$, G becomes much smaller.

In addition to the change of wave frequency due to background shear, the PSI of internal tides can also be influenced by the Doppler effect due to the background current (Richet et al., 2017). Namely, the intrinsic frequency M_2 of internal tides becomes $\omega_0 - \mathbf{k}_H \cdot \mathbf{U}$ in the frame of background current due to Doppler effect, where $\mathbf{k}_H$ is the horizontal wavenumber of internal tides. In the Tokara Strait, the propagation direction of the M_2 internal tides is generally opposite to the direction of the Kuroshio Current (Figure 4). Therefore, the frequency change due to the Doppler effect is $-\mathbf{k}_H \cdot \mathbf{U} = |\mathbf{k}_H| \cdot |\mathbf{U}|$. Here, we calculate the horizontal wavenumber of the M_2 internal tides according to the linear dispersion relation of internal tides:

$$\omega_0^2 = c_n^2 k_H^2 + f_0^2, \tag{17}$$

where c_n is the eigenspeed of the nth mode obtained by solving the eigenvalue problem with the stratification from model results (Gill, 1982). The mode-1 horizontal wavenumber in the Tokara Strait is approximately 5×10^{-5} m^{-1}, so the estimated frequency change is $|\mathbf{k}_H| \cdot |\mathbf{U}| = 1.3 \times 10^{-5}$ s^{-1} by assuming $|\mathbf{U}| = 0.25$ m/s as the depth-averaged speed of the Kuroshio Current following Masunaga et al. (2019). In the wake of the island chain southwest of Yakushima, the M_2 internal tides cannot generate subharmonic waves with the frequency $(\omega_0 + |\mathbf{k}_H| \cdot |\mathbf{U}|)/2$ via PSI in the positive vorticity band, since the local $\omega_{\min}$ is much higher than $(\omega_0 + |\mathbf{k}_H| \cdot |\mathbf{U}|)/2$. As a result, PSI in the Tokara Strait can be weakened. However, it should be noted that the Kuroshio-Topography interaction also generates near-inertial waves in this region. If the near-inertial waves generated by the two

mechanisms are out of phase, the weakening of the near-inertial waves generated by PSI also occurs. Hence, the Doppler effect is not the only possibility. In contrast, the situation is different for the Okinawa Trough where the M_2 internal tides propagate northwestward to the shallow shelf in the East China Sea, whereas the Kuroshio Current flows northeastward along the isobaths. Therefore, the frequency of internal tides is not shifted because the wave direction is almost perpendicular to the flow direction ($\mathbf{k}_H \cdot \mathbf{U} = 0$). As a result, this mechanism cannot explain the suppression of PSI in the Okinawa Trough.

Near-inertial waves can be advected by background currents. In Run-T, the region with high energy transfer rates in the Okinawa Trough has a length scale no more than 300 km along the Kuroshio Current direction. Because the reduction of near-inertial energy is mainly found in the upper ocean where the core of the Kuroshio Current is located (Figures 11b and 14b), a flow speed of 1 m/s is considered. Hence, the estimated advection time scale is 3.5 days. Such a time scale is much shorter than that for the growth of PSI as mentioned in Section 3.2. In other words, the near-inertial waves are easily advected downstream by the Kuroshio Current while the PSI develops slowly with the result that very little near-inertial energy accumulates in this region. On the basis of the above analyses, we believe that two mechanisms, that is, the change of $\omega_{\min}$ and the advection effect by the Kuroshio Current, could lead to the weakening of PSI in the study region. However, it is somewhat difficult to identify the dominant one because the two effects cannot be separated for the realistic Kuroshio Current.

5. Discussion

5.1. Generation of High-Frequency Internal Waves

As mentioned in Sections 3.2 and 4.1, in addition to the dominant near-inertial peak, another peak at the M_3 tidal frequency is also detectable. This implies the occurrence of nonlinear interaction between the M_2 internal tides and PSI-generated near-inertial waves. For further exploration, wavelet analysis is performed (Figure 5b). As shown in Figure 2b, the M_2 internal tides quickly reach a steady state within the first 10 days. Thereafter, with the development of PSI, large spectral density appears at the near-inertial frequency after 20 days. The developed near-inertial waves then interact with the M_2 internal tides so as to generate the M_3 internal tides. During this process, energy is transferred from the low-frequency to high-frequency internal waves, which has been observed by Sun and Pinkel (2012) and Yang et al. (2022). Moreover, by checking the two-dimensional wavenumber spectrum, we find that the M_3 waves satisfy the linear dispersion relation of internal waves, confirming that the generated M_3 waves are free internal waves rather than local perturbations.

Figure 16 shows the M_3 internal waves in Run-TK, which are extracted by using a bandpass filter with a cutoff frequency of [2.7 3.1] cpd (Figure 6a). Because the generation of the M_3 internal tides requires both the M_2 internal tides and near-inertial waves, they mainly appear in the Tokara Strait southwest of Yakushima Island (Figures 16a and 16b). In contrast, these high-frequency internal waves are absent in the deep Western Pacific. Although the M_3 internal tides are obviously weaker than the M_2 internal tides (Figure 16a), their dissipation rates are nearly comparable to those of the M_2 internal tides, especially in the northern part of the Tokara Strait (Figure 16b). Compared with the M_2 internal tides, the M_3 waves show high-mode features reflecting their complicated vertical structures, and thus contribute to the mixing despite their lower intensity. This result suggests that the role of high-frequency M_3 internal tides in driving mixing in this region cannot be neglected.

5.2. Implications of This Study

Intense turbulent mixing in the Tokara Strait has been evidenced by oceanic observations (Hasegawa et al., 2021; Tanaka et al., 2021; Tsutsumi et al., 2017). Here, we compare the calculated energy dissipation rates for Run-TK with microstructure observations in November 2015. More details about the observational experiment can be found in Tsutsumi et al. (2017). As shown in Figure 17, the calculated energy dissipation rates for Run-TK generally agree with the observations, not only in magnitude but also in spatial structure. Our model predicts the elevated mixing around seamounts in Transect I (Figures 17a and 17b) and downstream the Kuroshio Current in Transect II (Figures 17c and 17d). Additionally, the calculated energy dissipation rates around the Hirase Seamount are generally consistent with the observations from Hasegawa et al. (2021), which are shown in Supporting Information S1. These results provide further validity for our model results.

Previous studies have proposed several mechanisms responsible for the strong mixing in the Tokara Strait. Nagai et al. (2017, 2021) suggested that the high-wavenumber near-inertial waves excited by the Kuroshio-Topography

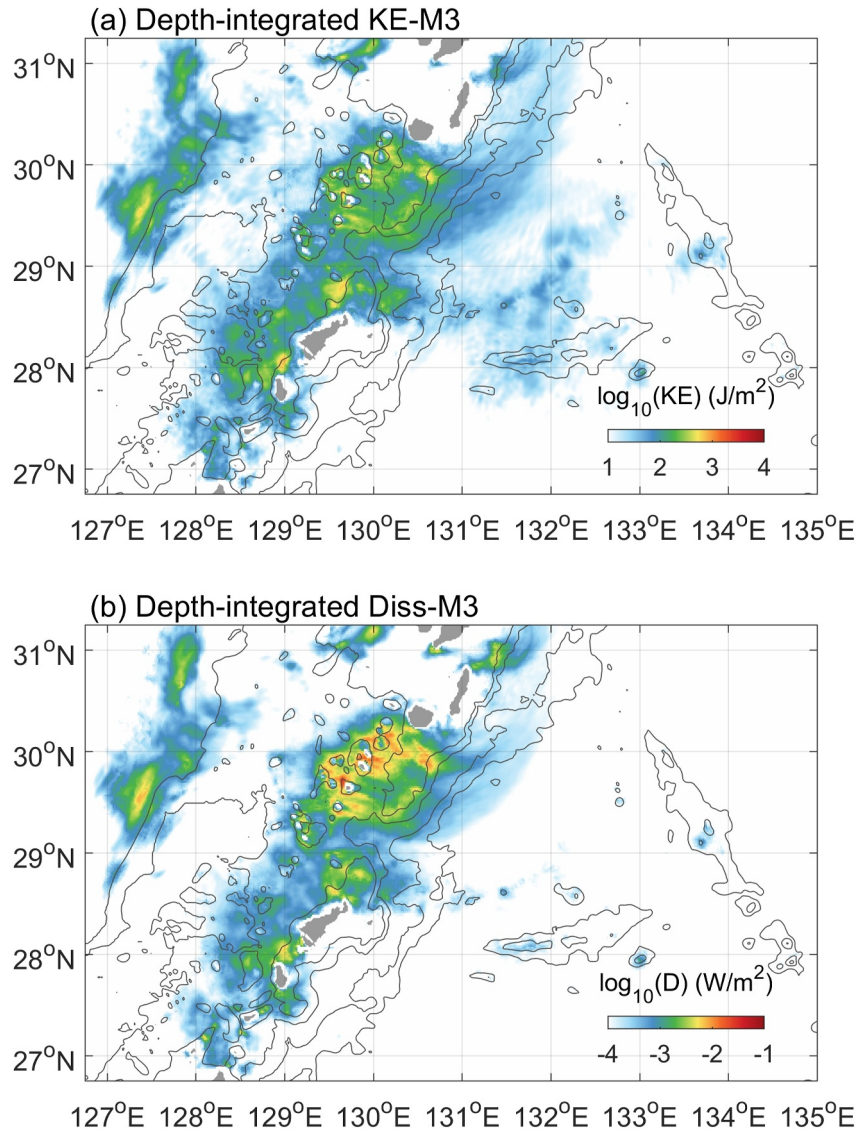

Figure 16. (a) Depth-integrated baroclinic kinetic energy (log form, shading, unit: J/m^2) and (b) energy dissipation rate (log form, shading, unit: W/m^2) of the M_3 internal tides in Run-TK. Gray contours in each panel denote 500, 1,000, 2,000, and 3,000 m isobaths.

interaction make a significant contribution. Hasegawa et al. (2021) observed the flow-separation and trains of the Kelvin-Helmholtz billows as the Kuroshio Current flows over a seamount, which enhances the mixing in the lee side of the topography. Inoue et al. (2024) and Takahashi et al. (2024) revealed that the sub-mesoscale vortex street and internal lee waves generated by Kuroshio and tidal currents jointly give rise to turbulence in topographic wake. Here, the results of this study provide another possible mechanism: PSI of the M_2 internal tides occurs at the critical latitude, which gives rise to the high-wavenumber near-inertial waves. Within the Kuroshio Current, the aforementioned processes along with PSI can contribute to mixing. It is difficult to identify the dominant one because they are nonlinearly intertwined, and the relative importance of each dynamical process is strongly dependent on the Kuroshio conditions (speed, path, and thickness), stratification, and bottom topographies. However, in the areas outside the narrow Kuroshio path, PSI makes a major contribution to mixing according to our model results. Hence, it is the composite flow including both the Kuroshio and tidal currents that fuels the turbulence in the Tokara Strait and adjacent regions.

Although this study focuses on PSI of the M_2 internal tides and the generated near-inertial waves in the Tokara Strait, it should be noted that other processes including the Kuroshio-topography and tidal current-topography

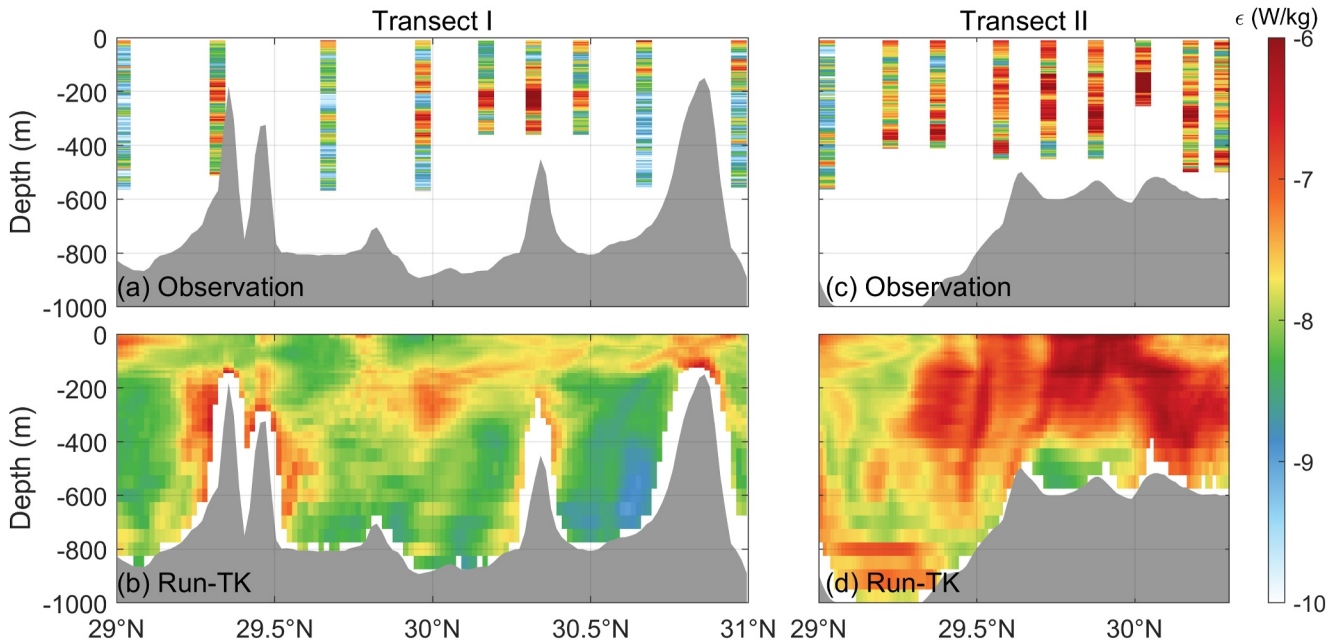

Figure 17. (a and c) Observed (Tsutsumi et al., 2017) and (b and d) calculated energy dissipation rates for Run-TK (log form, shadings, unit: W/kg) along Transects I and II. Bottom topographies are denoted by gray shadings.

interactions also result in near-inertial waves. These processes have been explored by He and Hibiya (2024) and Hibiya et al. (2024), which are also found in our model results. However, the situation becomes complicated when considering the composite flow with both Kuroshio and tidal currents, as indicated by the comparison among the results of Run-TK, Run-K, and Run-T (Section 3.2). The downstream near-inertial energy in Run-K decreases when tidal currents are introduced (Figure 6). He and Hibiya (2024) suggested that in the presence of steady flow, internal lee waves are excited by the composite flow superposed by the steady flow as well as near-inertial currents originated from the initial transient response; whereas the generated internal lee waves can in turn supply the near-inertial energy around the topography as they are Doppler shifted. This is the situation for Run-K. Nevertheless, in the presence of both Kuroshio and tidal currents in Run-TK, the background flow is time-varying rather than steady, thereby influencing the generation of internal lee waves depending on the direction and magnitude of tidal currents. Consequently, the supply to near-inertial energy is affected. This may be a possible explanation why less near-inertial energy is advected downstream by the Kuroshio Current in Run-TK.

6. Summary

In this study, PSI of the M_2 internal tides in the Tokara Strait is investigated by performing three-dimensional high-resolution simulations using the MITgcm. The simulated results are validated through comparison with those from several data sets. PSI of the M_2 internal tides is successfully reproduced in our simulation. The characteristics and energetics of near-inertial waves induced by PSI are analyzed, and the influence of the Kuroshio Current on PSI is revealed. The main conclusions of this study are listed as follows:

1. PSI of the M_2 internal tides occurs in the Tokara Strait, which is located at the M_2 critical latitude and generates strong near-inertial waves. The PSI-generated near-inertial waves are characterized by a horizontally layered structure of baroclinic velocities, which have much larger vertical wavenumbers and hence smaller vertical scales than the M_2 internal tides.
2. In PSI, the dominant energy balance is between the energy transfer from the M_2 internal tides into near-inertial waves and the dissipation of near-inertial waves. Both of them occur locally around the generation sites of internal tides. Near-inertial waves induce energy dissipation rates comparable to those of the M_2 internal tides around the topography, although they are weaker than the M_2 internal tides.
3. The presence of the Kuroshio Current suppresses PSI of the M_2 internal tides in the Okinawa Trough where the main body of the Kuroshio Current exists, causing reduced energy dissipation and transfer rates. Two

mechanisms could result in the weakening of PSI: one is the changing of minimum internal wave frequency caused by Kuroshio Current shear, whereas the other is the advection effect of the Kuroshio Current.

4. Near-inertial waves excited by PSI can further interact with the M_2 internal tides, generating the M_3 internal tides around the shelf break. Although these high-frequency internal tides are less energetic than the M_2 internal tides, they also cause considerable energy dissipation in the Tokara Strait.

Although PSI of the M_2 internal tides is reproduced by our model and analyzed in this study, the climatological Kuroshio Current is considered for simplification. In the Tokara Strait, the Kuroshio Current shows temporal variations in path and strength, which could lead to time-varying PSI in this region. Additionally, submesoscale features such as the inertial-symmetric instability caused by the Kuroshio-Topography interaction are not sufficiently resolved by the present model. How these processes affect PSI deserves further exploration but using a model with a much higher resolution. Moreover, although we find that near-inertial waves gain energy from both the semidiurnal internal tides and Kuroshio Current, the two energy pathways are considered individually. Recently studies by He and Hibiya (2024) and Hibiya et al. (2024) suggested an important role of composite flow in supplying near-inertial energy via modulating the generated internal lee waves by the Doppler effect. Such effect on near-inertial waves in the Tokara Strait will be explored in future work. Despite the above limitations, this study indicates an important process contributing to strong mixing in the Tokara Strait. PSI of the semidiurnal internal tides majorly contributes to mixing in the Tokara Strait and adjacent regions outside the Kuroshio path, but may equally contribute to mixing as other processes locally around the topographies along the Kuroshio path (Sections 3.2 and 3.4). Moreover, this study provides essential implications on the energy cascade of internal tides, which should be incorporated into the corresponding parameterizations.

Data Availability Statement

ETOPO1 data can be downloaded from https://www.ngdc.noaa.gov/mgg/global (Amante & Eakins, 2009). The initial stratification is extracted from WOA13 (https://www.ncei.noaa.gov/products/world-ocean-atlas, Locarnini et al., 2013; Zweng et al., 2013). OTIS can be downloaded from https://www.tpxo.net/ (Egbert & Erofeeva, 2002). FORA data set can be accessed at http://metadata.diasjp.net/dmm/doc/FORA_WNP30_JAMSTEC_MRI-DIAS-en.html (Usui et al., 2017). Tidal gauge observations are downloaded from the Japan Oceanographic Data Center (https://www.jodc.go.jp/vpage/tide.html, JODC, 2024). The altimetry results of internal tides are created by Dr. Edward D. Zaron and can be downloaded from https://ingria.ceoas.oregonstate.edu/~zarone/downloads.html (Zaron, 2019). The code of MITgcm can be obtained from http://mitgcm.org/ (Marshall et al., 1997) and the model configuration can be found at https://figshare.com/articles/software/mitgcm_config/21781550 (Wang, 2022).

Acknowledgments
The authors deeply thank Drs. Toshiyuki Hibiya, Yohei Onuki, and an anonymous reviewer as well as the editor Dr. Takeyoshi Nagai for their insightful comments which greatly improve this paper. Fruitful discussions with Dr. Qun Li are gratefully acknowledged. S. Wang and X. Guo were supported by the JSPS Postdoctoral Fellowships for Research in Japan (Grant 23KF0056), Grant-in-Aid for Scientific Research (MEXT KAKENHI Grant 22H05206), and Japan Fisheries Research and Education Agency. A. Cao was supported by the National Natural Science Foundation of China (Grant 42176002), the China Scholarship Council (Grant 202006325025), and the Funding of ZJU Tang Scholar.

References

Alford, M. H. (2003). Redistribution of energy available for ocean mixing by long-range propagation of internal waves. *Nature*, *423*(6936), 159–162. https://doi.org/10.1038/nature01628

Alford, M. H. (2008). Observations of parametric subharmonic instability of the diurnal internal tide in the South China Sea. *Geophysical Research Letters*, *35*(15), L15602. https://doi.org/10.1029/2008gl034720

Alford, M. H., MacKinnon, J. A., Zhao, Z., Pinkel, R., Klymak, J., & Peacock, T. (2007). Internal waves across the Pacific. *Geophysical Research Letters*, *34*(24). https://doi.org/10.1029/2007gl031566

Amante, C., & Eakins, B. W. (2009). ETOPO1 1 arc-minute global relief model: Procedures, data sources and analysis [Dataset]. NOAA Technical Memorandum NESDIS NGDC-24. National Geophysical Data Center, NOAA. https://www.ngdc.noaa.gov/mgg/global

Ansong, J. K., Arbic, B. K., Simmons, H. L., Alford, M. H., Buijsman, M. C., Timko, P. G., et al. (2018). Geographical distribution of diurnal and semidiurnal parametric subharmonic instability in a global ocean circulation model. *Journal of Physical Oceanography*, *48*(6), 1409–1431. https://doi.org/10.1175/jpo-d-17-0164.1

Cole, S. T., Rudnick, D. L., Hodges, B. A., & Martin, J. P. (2009). Observations of tidal internal wave beams at Kauai Channel, Hawaii. *Journal of Physical Oceanography*, *39*(2), 421–436. https://doi.org/10.1175/2008jpo3937.1

Delorme, B. L., & Thomas, L. N. (2023). Turbulence generated through critical reflection of internal waves off the seafloor due to nontraditional effects. *Journal of Physical Oceanography*, *53*(3), 699–718. https://doi.org/10.1175/jpo-d-22-0077.1

Durán Gómez, G. S., & Nagai, T. (2022). Elevated nutrient supply caused by the approaching Kuroshio to the southern coast of Japan. *Frontiers in Marine Science*, *9*, 842155. https://doi.org/10.3389/fmars.2022.842155

Egbert, G. D., & Erofeeva, S. Y. (2002). Efficient inverse modeling of barotropic ocean tides [Software]. *Journal of Atmospheric and Oceanic Technology*, *19*(2), 183–204. https://doi.org/10.1175/1520-0426(2002)019<0183:eimobo>2.0.co;2

Garrett, C. (2003). Mixing with latitude. *Nature*, *422*(6931), 477–478. https://doi.org/10.1038/422477a

Garrett, C., & Kunze, E. (2007). Internal tide generation in the deep ocean. *Annual Review of Fluid Mechanics*, *39*(1), 57–87. https://doi.org/10.1146/annurev.fluid.39.050905.110227

Gerkema, T., Staquet, C., & Bouruet-Aubertot, P. (2006). Decay of semi-diurnal internal-tide beams due to subharmonic resonance. *Geophysical Research Letters*, *33*(8). https://doi.org/10.1029/2005gl025105

Gerkema, T., & Zimmerman, J. T. F. (2008). *An introduction to internal waves* (p. 207). Royal NIOZ Lecture Notes.
Gill, A. E. (1982). *Atmosphere-ocean dynamics* (p. 662). Academic Press.
Girton, J., Chinn, B., & Alford, M. (2011). Internal wave climates of the Philippine Seas. *Oceanography*, *24*(01), 100–111. https://doi.org/10.5670/oceanog.2011.07
Hasegawa, D., Matsuno, T., Tsutsumi, E., Senjyu, T., Endoh, T., Tanaka, T., et al. (2021). How a small reef in the Kuroshio cultivates the ocean. *Geophysical Research Letters*, *48*(7). https://doi.org/10.1029/2020gl092063
Hazewinkel, J., & Winters, K. B. (2011). PSI of the internal tide on a β plane: Flux divergence and near-inertial wave propagation. *Journal of Physical Oceanography*, *41*(9), 1673–1682. https://doi.org/10.1175/2011jpo4605.1
He, Y., & Hibiya, T. (2024). The vertical structure of internal lee wave-driven benthic mixing hotspots. *Journal of Physical Oceanography*, *54*(1), 253–263. https://doi.org/10.1175/jpo-d-22-0268.1
Hibiya, T., & Nagasawa, M. (2004). Latitudinal dependence of diapycnal diffusivity in the thermocline estimated using a finescale parameterization. *Geophysical Research Letters*, *31*(1), L01301. https://doi.org/10.1029/2003gl017998
Hibiya, T., Nagasawa, M., & Niwa, Y. (2002). Nonlinear energy transfer within the oceanic internal wave spectrum at mid and high latitudes. *Journal of Geophysical Research*, *107*(C11), 3207. https://doi.org/10.1029/2001jc001210
Hibiya, T., Nagasawa, M., & Niwa, Y. (2006). Global mapping of diapycnal diffusivity in the deep ocean based on the results of expendable current profiler (XCP) surveys. *Geophysical Research Letters*, *33*(3), L03611. https://doi.org/10.1029/2005gl025218
Hibiya, T., Nagasawa, M., & Niwa, Y. (2007). Latitudinal dependence of diapycnal diffusivity in the thermocline observed using a microstructure profiler. *Geophysical Research Letters*, *34*(24). https://doi.org/10.1029/2007gl032323
Hibiya, T., Niwa, Y., & Fujiwara, K. (1998). Numerical experiments of nonlinear energy transfer within the oceanic internal wave spectrum. *Journal of Geophysical Research*, *103*(C9), 18715–18772. https://doi.org/10.1029/98jc01362
Hibiya, T., Tanaka, Y., Nagai, T., & Hirano, Y. (2024). Revisiting tide-induced near-field mixing in the Abyssal Ocean. *Geophysical Research Letters*. (in press).
Inoue, R., Tsutsumi, E., & Nakamura, H. (2024). Numerical simulation of the Kuroshio flowing over the Hirase seamount in the Tokara Strait in Autumn: Tidal vortex shedding in a baroclinic jet. *Journal of Physical Oceanography*, *54*(1), 153–172. https://doi.org/10.1175/jpo-d-23-0050.1
Iwamae, N., & Hibiya, T. (2012). Numerical study of tide-induced mixing over rough bathymetry in the abyssal ocean. *Journal of Oceanography*, *68*(1), 195–203. https://doi.org/10.1007/s10872-011-0088-2
Jan, S., Chern, C., Wang, J., & Chao, S. (2007). Generation of diurnal K1 internal tide in the Luzon Strait and its influence on surface tide in the South China Sea. *Journal of Geophysical Research*, *112*(C6). https://doi.org/10.1029/2006jc004003
Jayne, S. R., Laurent, L. S., & Gille, S. T. (2004). Connections between ocean bottom topography and Earth's climate. *Oceanography*, *17*(1), 65–74. https://doi.org/10.5670/oceanog.2004.68
JODC. (2024). Tide (hour tidal height) data. Retrieved from https://www.jodc.go.jp/vpage/tide.html
Kerry, C. G., Powell, B. S., & Carter, G. S. (2013). Effects of remote generation sites on model estimates of M_2 internal tides in the Philippine sea. *Journal of Physical Oceanography*, *43*(1), 187–204. https://doi.org/10.1175/jpo-d-12-081.1
Liu, K., & Zhao, Z. (2020). Disintegration of the K1 internal tide in the South China sea due to parametric subharmonic instability. *Journal of Physical Oceanography*, *50*(12), 3605–3622. https://doi.org/10.1175/jpo-d-19-0320.1
Liu, Z. J., Nakamura, H., Zhu, X. H., Nishina, A., Guo, X., & Dong, M. (2019). Tempo-spatial variations of the Kuroshio current in the Tokara Strait based on long-term Ferryboat ADCP data. *Journal of Geophysical Research: Oceans*, *124*(8), 6030–6049. https://doi.org/10.1029/2018jc014771
Locarnini, R. A., Mishonov, A. V., Antonov, J. I., Boyer, T. P., Garcia, H. E., Baranova, O. K., et al. (2013) In S. Levitus, (Ed.), & A. Mishonov (Technical Ed.), *World Ocean Atlas 2013, volume 1: Temperature*. [Dataset]. (p. 40). NOAA Atlas NESDIS 73. Retrieved from https://www.ncei.noaa.gov/products/world-ocean-atlas
Mackinnon, J. A., Alford, M. H., Ansong, J. K., Arbic, B. K., Barna, A., Briegleb, B. P., et al. (2017). Climate process team on internal wave-driven ocean mixing. *Bulletin of the American Meteorological Society*, *98*(11), 2429–2454. https://doi.org/10.1175/bams-d-16-0030.1
MacKinnon, J. A., Alford, M. H., Pinkel, R., Klymak, J., & Zhao, Z. (2013). The latitudinal dependence of shear and mixing in the Pacific transiting the critical latitude for PSI. *Journal of Physical Oceanography*, *43*(1), 3–16. https://doi.org/10.1175/jpo-d-11-0107.1
MacKinnon, J. A., Alford, M. H., Sun, O., Pinkel, R., Zhao, Z., & Klymak, J. (2013). Parametric subharmonic instability of the internal tide at 29°N. *Journal of Physical Oceanography*, *43*(1), 17–28. https://doi.org/10.1175/jpo-d-11-0108.1
MacKinnon, J. A., & Winters, K. B. (2005). Subtropical catastrophe: Significant loss of low-mode tidal energy at 28.9°. *Geophysical Research Letters*, *32*(15). https://doi.org/10.1029/2005gl023376
Marshall, J., Adcroft, A., Hill, C., Perelman, L., & Heisey, C. (1997). A finite-volume, incompressible Navier-stokes model for studies of the ocean on parallel computers [Software]. *Journal of Geophysical Research*, *102*(C3), 5753–5766. https://doi.org/10.1029/96jc02775
Masunaga, E., Uchiyama, Y., & Yamazaki, H. (2019). Strong internal waves generated by the interaction of the Kuroshio and tides over a shallow ridge. *Journal of Physical Oceanography*, *49*(11), 2917–2934. https://doi.org/10.1175/jpo-d-18-0238.1
McComas, C. H., & Bretherton, F. P. (1977). Resonant interaction of oceanic internal waves. *Journal of Geophysical Research*, *82*(9), 1397–1412. https://doi.org/10.1029/jc082i009p01397
Munk, W., & Wunsch, C. (1998). Abyssal recipes II: Energetics of tidal and wind mixing. *Deep Sea Research Part I: Oceanographic Research Papers*, *45*(12), 1977–2010. https://doi.org/10.1016/s0967-0637(98)00070-3
Nagai, T., Hasegawa, D., Tanaka, T., Nakamura, H., Tsutsumi, E., Inoue, R., & Yamashiro, T. (2017). First evidence of coherent bands of strong turbulent layers associated with high-wavenumber internal-wave shear in the upstream Kuroshio. *Scientific Reports*, *7*(1), 14555. https://doi.org/10.1038/s41598-017-15167-1
Nagai, T., Hasegawa, D., Tsutsumi, E., Nakamura, H., Nishina, A., Senjyu, T., et al. (2021). The Kuroshio flowing over seamounts and associated submesoscale flows drive 100-km-wide 100-1000-fold enhancement of turbulence. *Communications Earth & Environment*, *2*(1), 170. https://doi.org/10.1038/s43247-021-00230-7
Nagai, T., & Hibiya, T. (2015). Internal tides and associated vertical mixing in the Indonesian Archipelago. *Journal of Geophysical Research: Oceans*, *120*(5), 3373–3390. https://doi.org/10.1002/2014jc010592
Nagai, T., Tandon, A., Kunze, E., & Mahadevan, A. (2015). Spontaneous generation of near-inertial waves by the Kuroshio front. *Journal of Physical Oceanography*, *45*(9), 2381–2406. https://doi.org/10.1175/jpo-d-14-0086.1
Nagasawa, M., Hibiya, T., Niwa, Y., Watanabe, M., Isoda, Y., Takagi, S., & Kamei, Y. (2002). Distribution of fine-scale shear in the deep waters of the North Pacific obtained using expendable current profilers. *Journal of Geophysical Research*, *107*(C12), 3221. https://doi.org/10.1029/2002jc001376
Nash, J. D., Alford, M. H., & Kunze, E. (2005). Estimating internal wave energy fluxes in the ocean. *Journal of Atmospheric and Oceanic Technology*, *22*(10), 1551–1570. https://doi.org/10.1175/jtech1784.1

Nelson, A. D., Arbic, B. K., Menemenlis, D., Peltier, W. R., Alford, M. H., Grisouard, N., & Klymak, J. M. (2020). Improved internal wave spectral continuum in a regional ocean model. *Journal of Geophysical Research: Oceans*, *125*(5), e2019JC015974. https://doi.org/10.1029/2019jc015974

Nikurashin, M., & Legg, S. (2011). A mechanism for local dissipation of internal tides generated at rough topography. *Journal of Physical Oceanography*, *41*(2), 378–395. https://doi.org/10.1175/2010jpo4522.1

Niwa, Y., & Hibiya, T. (2004). Three-dimensional numerical simulation of M_2 internal tides in the East China Sea. *Journal of Geophysical Research*, *109*(C4). https://doi.org/10.1029/2003jc001923

Niwa, Y., & Hibiya, T. (2011). Estimation of baroclinic tide energy available for deep ocean mixing based on three-dimensional global numerical simulations. *Journal of Oceanography*, *67*(4), 493–502. https://doi.org/10.1007/s10872-011-0052-1

Oka, A., & Niwa, Y. (2013). Pacific deep circulation and ventilation controlled by tidal mixing away from the sea bottom. *Nature Communications*, *4*(1), 2419. https://doi.org/10.1038/ncomms3419

Onuki, Y., & Hibiya, T. (2015). Excitation mechanism of near-inertial waves in baroclinic tidal flow caused by parametric subharmonic instability. *Ocean Dynamics*, *65*(1), 107–113. https://doi.org/10.1007/s10236-014-0789-3

Onuki, Y., & Hibiya, T. (2018). Decay rates of internal tides estimated by an improved wave–wave interaction analysis. *Journal of Physical Oceanography*, *48*(11), 2689–2701. https://doi.org/10.1175/jpo-d-17-0278.1

Pickering, A., & Alford, M. H. (2012). Velocity structure of internal tide beams emanating from Kaena Ridge, Hawaii. *Journal of Physical Oceanography*, *42*(6), 1039–1044. https://doi.org/10.1175/jpo-d-12-018.1

Rainville, L., Johnston, T. M. S., Carter, G. S., Merrifield, M. A., Pinkel, R., Worcester, P. F., & Dushaw, B. D. (2010). Interference pattern and propagation of the M_2 internal tide south of the Hawaiian ridge. *Journal of Physical Oceanography*, *40*(2), 311–325. https://doi.org/10.1175/2009jpo4256.1

Richet, O., Chomaz, J.-M., & Muller, C. (2018). Internal tide dissipation at topography: Triadic resonant instability equatorward and evanescent waves poleward of the critical latitude. *Journal of Geophysical Research: Oceans*, *123*(9), 6136–6155. https://doi.org/10.1029/2017jc013591

Richet, O., Muller, C., & Chomaz, J. M. (2017). Impact of a mean current on the internal tide energy dissipation at the critical latitude. *Journal of Physical Oceanography*, *47*(6), 1457–1472. https://doi.org/10.1175/jpo-d-16-0197.1

Schlosser, T. L., Jones, N. L., Bluteau, C. E., Alford, M. H., Ivey, G. N., & Lucas, A. J. (2019). Generation and propagation of near-inertial waves in a baroclinic current on the Tasmanian shelf. *Journal of Physical Oceanography*, *49*(10), 2653–2667. https://doi.org/10.1175/jpo-d-18-0208.1

Simmons, H. L. (2008). Spectral modification and geographic redistribution of the semi-diurnal internal tide. *Ocean Modelling*, *21*(3–4), 126–138. https://doi.org/10.1016/j.ocemod.2008.01.002

Simmons, H. L., Hallberg, R. W., & Arbic, B. K. (2004). Internal wave generation in a global baroclinic tide model. *Deep Sea Research Part II: Topical Studies in Oceanography*, *51*(25–26), 3043–3068. https://doi.org/10.1016/j.dsr2.2004.09.015

St. Laurent, L., & Garrett, C. (2002). The role of internal tides in mixing the deep ocean. *Journal of Physical Oceanography*, *32*(10), 2882–2899. https://doi.org/10.1175/1520-0485(2002)032<2882:troiti>2.0.co;2

Sun, O. M., & Pinkel, R. (2012). Energy transfer from high-shear, low-frequency internal waves to high-frequency waves near Kaena ridge, Hawaii. *Journal of Physical Oceanography*, *42*(9), 1524–1547. https://doi.org/10.1175/jpo-d-11-0117.1

Takahashi, A., Lien, R., Kunze, E., Ma, B., Nakamura, H., Nishina, A., et al. (2024). Energetic stratified turbulence generated by Kuroshio–seamount interactions in Tokara Strait. *Journal of Physical Oceanography*, *54*(2), 461–484. https://doi.org/10.1175/jpo-d-22-0242.1

Tanaka, T., Hasegawa, D., Yasuda, I., Yanagimoto, D., Fujio, S., Nakamura, H., et al. (2021). Enhanced vertical turbulent nitrate flux in the intermediate layer of the Kuroshio in the Tokara Strait. *Journal of Oceanography*, *77*(1), 45–53. https://doi.org/10.1007/s10872-020-00581-3

Tanaka, Y., Hibiya, T., Niwa, Y., & Iwamae, N. (2010). Numerical study of K1 internal tides in the Kuril straits. *Journal of Geophysical Research*, *115*(C9), C09016. https://doi.org/10.1029/2009jc005903

Thomas, L. N., & Taylor, J. R. (2014). Damping of inertial motions by parametric subharmonic instability in baroclinic currents. *Journal of Fluid Mechanics*, *743*, 280–294. https://doi.org/10.1017/jfm.2014.29

Tsutsumi, E., Matsuno, T., Lien, R. C., Nakamura, H., Senjyu, T., & Guo, X. (2017). Turbulent mixing within the Kuroshio in the Tokara Strait. *Journal of Geophysical Research: Oceans*, *122*(9), 7082–7094. https://doi.org/10.1002/2017jc013049

Usui, N., Wakamatsu, T., Tanaka, Y., Hirose, N., Toyoda, T., Nishikawa, S., et al. (2017). Four-dimensional Variational Ocean Reanalysis: A 30-year high-resolution dataset in the western north Pacific (FORA-WNP30) [Dataset]. *Journal of Oceanography*, *73*(2), 205–233. https://doi.org/10.1007/s10872-016-0398-5

Varlamov, S. M., Guo, X., Miyama, T., Ichikawa, K., Waseda, T., & Miyazawa, Y. (2015). M2 baroclinic tide variability modulated by the ocean circulation south of Japan. *Journal of Geophysical Research: Oceans*, *120*(5), 3681–3710. https://doi.org/10.1002/2015jc010739

Vic, C., Naveira Garabato, A. C., Green, J. A. M., Waterhouse, A. F., Zhao, Z., Melet, A., et al. (2019). Deep-ocean mixing driven by small-scale internal tides. *Nature Communications*, *10*(1), 2099. https://doi.org/10.1038/s41467-019-10149-5

Wang, S. (2022). mitgcm_config [Software]. *figshare*. https://doi.org/10.6084/m9.figshare.21781550.v1

Wang, S., Cao, A., Chen, X., Li, Q., & Song, J. (2021). On the resonant triad interaction over mid-ocean ridges. *Ocean Modelling*, *158*, 101734. https://doi.org/10.1016/j.ocemod.2020.101734

Wang, S., Cao, A., Liang, X., Chen, X., & Meng, J. (2021). Impact of background geostrophic currents with vorticity on resonant triad interaction over mid-ocean ridges. *Journal of Geophysical Research: Oceans*, *126*(4). https://doi.org/10.1029/2021jc017227

Wang, Y., Xu, Z., Yin, B., Hou, Y., & Chang, H. (2018). Long-range radiation and interference pattern of multisource M2 internal tides in the Philippine sea. *Journal of Geophysical Research: Oceans*, *123*(8), 5091–5112. https://doi.org/10.1029/2018jc013910

Whalen, C. B., de Lavergne, C., Naveira Garabato, A. C., Klymak, J. M., MacKinnon, J. A., & Sheen, K. L. (2020). Internal wave-driven mixing: Governing processes and consequences for climate. *Nature Reviews Earth & Environment*, *1*(11), 606–621. https://doi.org/10.1038/s43017-020-0097-z

Whitt, D. B., & Thomas, L. N. (2013). Near-inertial waves in strongly baroclinic currents. *Journal of Physical Oceanography*, *43*(4), 706–725. https://doi.org/10.1175/jpo-d-12-0132.1

Yang, W., Hibiya, T., Tanaka, Y., Zhao, L., & Wei, H. (2018). Modification of parametric subharmonic instability in the presence of background geostrophic currents. *Geophysical Research Letters*, *45*(23), 12957–12962. https://doi.org/10.1029/2018gl080183

Yang, W., Wei, H., & Zhao, L. (2020). Parametric subharmonic instability of the semidiurnal internal tides at the East China Sea shelf slope. *Journal of Physical Oceanography*, *50*(4), 907–920. https://doi.org/10.1175/jpo-d-19-0163.1

Yang, W., Wei, H., & Zhao, L. (2022). Energy transfer from PSI-generated M1 subharmonic waves to high-frequency internal waves. *Geophysical Research Letters*, *49*(2). https://doi.org/10.1029/2021gl095618

Zaron, E. D. (2019). Baroclinic tidal sea level from exact-repeat mission altimetry [Dataset]. *Journal of Physical Oceanography*, *49*(1), 193–210. https://doi.org/10.1175/jpo-d-18-0127.1

Zhao, Z. (2014). Internal tide radiation from the Luzon Strait. *Journal of Geophysical Research: Oceans*, *119*(8), 5434–5448. https://doi.org/10.1002/2014jc010014

Zhao, Z. (2019). Mapping internal tides from satellite altimetry without blind directions. *Journal of Geophysical Research: Oceans*, *124*(12), 8605–8625. https://doi.org/10.1029/2019jc015507

Zhao, Z., Alford, M. H., Girton, J. B., Rainville, L., & Simmons, H. L. (2016). Global observations of open-ocean mode-1 M2 internal tides. *Journal of Physical Oceanography*, *46*(6), 1657–1684. https://doi.org/10.1175/jpo-d-15-0105.1

Zhao, Z., Alford, M. H., MacKinnon, J. A., & Pinkel, R. (2010). Long-range propagation of the semidiurnal internal tide from the Hawaiian ridge. *Journal of Physical Oceanography*, *40*(4), 713–736. https://doi.org/10.1175/2009jpo4207.1

Zweng, M. M., Reagan, J. R., Antonov, J. I., Locarnini, R. A., Mishonov, A. V., Boyer, T. P., et al. (2013). [Dataset]. In S. Levitus, & A. Mishonov Technical (Eds.), *World Ocean Atlas 2013, volume 2: Salinity*. (Vol. 74, p. 39). NOAA Atlas NESDIS. Retrieved from https://www.ncei.noaa.gov/products/world-ocean-atlas

References From the Supporting Information

Carter, G. S., & Gregg, M. C. (2006). Persistent near-diurnal internal waves observed above a site of M_2 barotropic-to-baroclinic conversion. *Journal of Physical Oceanography*, *36*(6), 1136–1147. https://doi.org/10.1175/jpo2884.1

Kundu, P. K., & Cohen, I. M. (2002). *Fluid mechanics* (2nd ed.). Academic Press.730

Pedlosky, J. (2003). *Waves in the ocean and atmosphere: Introduction to wave dynamics* (p. 264). Springer.

Xie, X., Shang, X., van Haren, H., & Chen, G. (2013). Observations of enhanced nonlinear instability in the surface reflection of internal tides. *Geophysical Research Letters*, *40*(8), 1580–1586. https://doi.org/10.1002/grl.50322